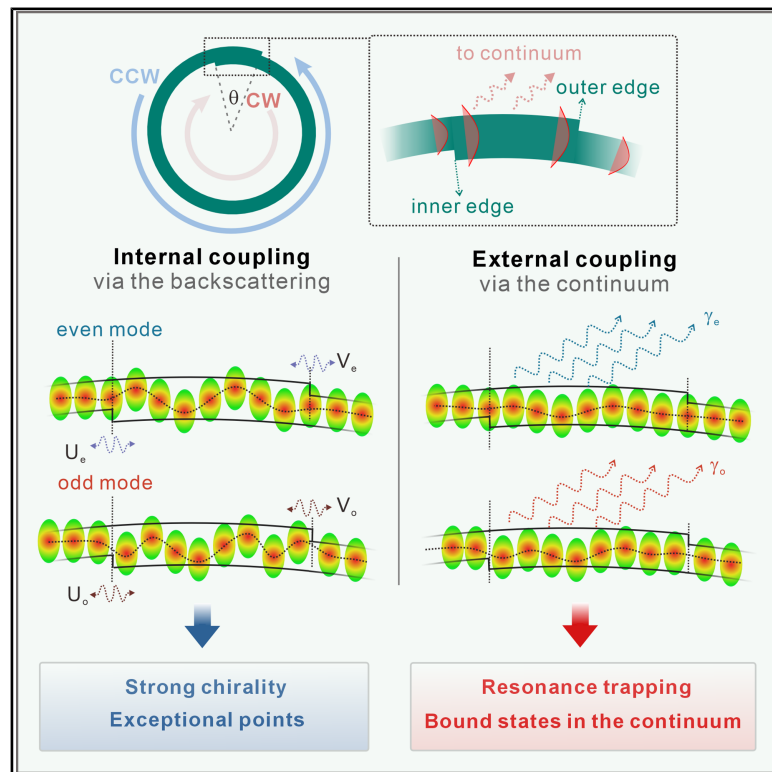


# Reconfigurable resonance trapping in single optical microresonators

## Graphical abstract



## Authors

Jin Li, Min Tang, Xiaoyu Wang, ...,  
Qinghai Song, Oliver G. Schmidt,  
Jiawei Wang

## Correspondence

wangjw7@hit.edu.cn

## In brief

While external coupling via the continuum is of fundamental importance, its role in optical microresonators remains largely unexplored. Li et al. reveal how the coupling mechanism operates in single microresonators, enabling resonance trapping and controlled light emission. These findings provide new insights into non-Hermitian physics across diverse systems.

## Highlights

- A generalized theory linking internal and external coupling in single resonators
- Geometric parameters enabling control of corresponding coupling strengths
- Experimental observation of resonance trapping from external coupling



## Article

# Reconfigurable resonance trapping in single optical microresonators

Jin Li,<sup>1,8</sup> Min Tang,<sup>2,8</sup> Xiaoyu Wang,<sup>3</sup> Christian N. Saggau,<sup>4,5</sup> Yin Yin,<sup>6</sup> Libo Ma,<sup>2</sup> Qinghai Song,<sup>1</sup> Oliver G. Schmidt,<sup>7</sup> and Jiawei Wang<sup>1,9,\*</sup>

<sup>1</sup>School of Integrated Circuits, Harbin Institute of Technology (Shenzhen), Shenzhen 518055, China

<sup>2</sup>Leibniz Institute for Solid State and Materials Research Dresden, 01069 Dresden, Germany

<sup>3</sup>School of Physics and Optoelectronic Engineering, Hainan University, Haikou 570228, China

<sup>4</sup>DTU Electro, Department of Electrical and Photonics Engineering, Technical University of Denmark, 2800 Lyngby, Denmark

<sup>5</sup>Center for Silicon Photonics for Optical Communications (SPOC), Technical University of Denmark, 1057 Lyngby, Denmark

<sup>6</sup>School of Materials Science and Engineering, Jiangsu University, Zhenjiang 212013, China

<sup>7</sup>Research Center for Materials, Architectures and Integration of Nanomembranes (MAIN), Technische Universität Chemnitz, Rosenbergstrasse 6, 09126 Chemnitz, Germany

<sup>8</sup>These authors contributed equally

<sup>9</sup>Lead contact

\*Correspondence: [wangjw7@hit.edu.cn](mailto:wangjw7@hit.edu.cn)

<https://doi.org/10.1016/j.newton.2025.100171>

**ACCESSIBLE OVERVIEW** Controlling how light waves interact with their surroundings is crucial for both scientific discovery and modern technologies. In optics, micron-sized ring-shaped resonators are adopted to trap light in whispering gallery resonances, where pairs of nearly identical light waves circulate around the boundary. While most studies have focused on how these resonant modes interact inside the ring, how they escape and couple via the “continuum” in the outside world is largely ignored. This study revisits this classic problem using a versatile theoretical framework, revealing how internal and external coupling can be connected. By engineering a microring with a strategically mismatched segment, we demonstrate precise control over these interactions, observing “resonance trapping,” a phenomenon where certain light waves become confined, dramatically reducing their energy loss. These findings, confirmed by experiments using spiral-shaped microtubes, could lead to better regulation of light emission, precision in optical sensors, and advances in quantum technologies. Beyond optics, this work provides a blueprint for studying wave behavior in electronic, mechanical, and hybrid systems, opening doors to innovations across physics and engineering.

## SUMMARY

External coupling via the continuum, a general concept in non-Hermitian physics, underpins fascinating phenomena such as bound states in the continuum and the Kerker effect. In optics, investigations of parametric bound states have been extended from multi-resonator systems to single units, such as supercavity modes in a Mie resonator. For single high-Q optical microresonators, prior research has primarily focused on internal coupling within the residing mode pair with broken degeneracy. Here, we revisit this classical two-mode coupling model by revealing its subtle connection to mode dissipation through the radiation continuum as a hidden dimension. This implication gets exemplified in a regular microring resonator with a mode-mismatch segment, enabling reconfigurable internal and external coupling. Furthermore, external coupling-induced resonance trapping features coherently suppressed decay channels. As a demonstration, tailoring spontaneous emission via resonance trapping is experimentally observed in rolled-up microresonators. We envisage that elucidating external coupling in single resonators will offer new perspectives for advancing non-Hermitian photonics and understanding resonances spanning mechanical, photonic, electronic, and hybrid systems.

## INTRODUCTION

Understanding open physical systems in reality has been a thriving area, with optics emerging as one of the most versatile

platforms.<sup>1–4</sup> Optical bound states exhibit remarkable abilities to trap electromagnetic waves within the radiation continuum, with recent studies advancing from multi-resonator<sup>5</sup> systems to isolated ones.<sup>6</sup> A notable example is the realization of



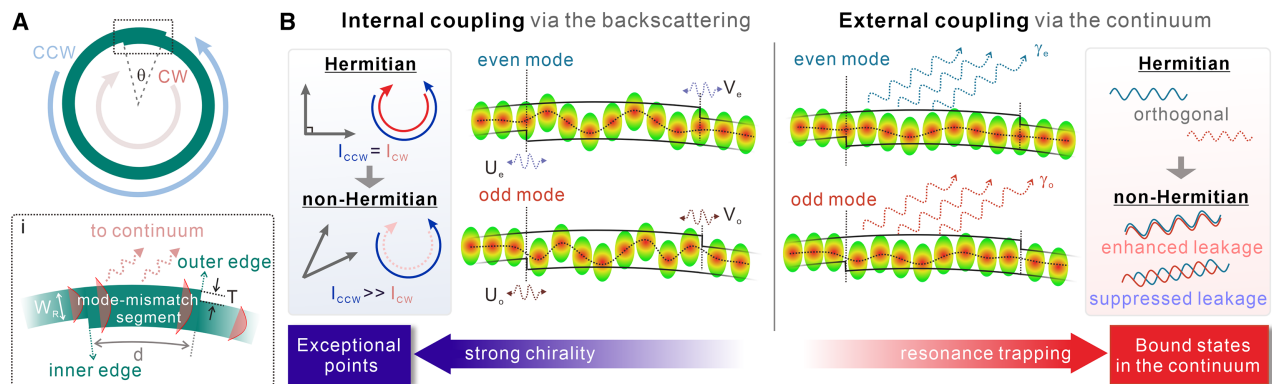


**Figure 1. Mode coupling in an asymmetric microring resonator**

(A) Schematic of an asymmetric ring resonator. The geometry can be described by a spiral function  $\rho(\psi) = R + \frac{T}{2\pi}\psi$ , where  $T$  is the lateral offset between the regular segment and the mode-mismatch segment, and  $\psi$  is the azimuthal angle. The winding angle  $\theta$  between 0 and  $2\pi$  quantifies the relative azimuthal position of two spiral edges. Hence, the length of the mode-mismatch segment  $d$  equals  $R\theta$ .  $W_R$  is the width of the regular waveguiding segment. Inset: enlarged view around the mode-mismatch segment between the outer and inner edges.

(B) Schematics around the mode-mismatch segment showing the induced internal (left) and external (right) coupling and their associated phenomena due to the non-Hermiticity. At left is illustrated the differences in eigenvectors (left) and the weights of CW and CCW components (right) in Hermitian and non-Hermitian systems; at right is illustrated the differences in radiation into the continuum.

“supercavity modes” in a Mie resonator through parametric tuning,<sup>7</sup> where bound states in the continuum emerge from the interference of two<sup>7–11</sup> nearly orthogonal modes within the resonator that couple predominantly in the external radiation field.<sup>12</sup> In addition to subwavelength resonators, whispering gallery mode (WGM) microresonators have garnered significant attention as energy-non-conserving systems, offering exceptional flexibility for tuning gain and loss conditions.<sup>1</sup> Previous research has primarily explored mode interactions between neighboring WGM resonators, unveiling intriguing phenomena such as parity-time symmetry,<sup>1,13,14</sup> exceptional points (EPs),<sup>2–4</sup> and all-optical electromagnetically induced transparency.<sup>7,12</sup> Moreover, the non-Hermiticity of single-WGM-resonator systems can also be tuned, enabling explorations in a simplified and compact framework.

For a single WGM resonator, the non-Hermitian degeneracy can be manipulated via introducing local defects (e.g., Rayleigh<sup>15–17</sup> or Mie scatterers<sup>18</sup>) in the vicinity of the boundary. In particular, via the well-established “two-scatterers” scheme,<sup>19,20</sup> the pair of eigenmodes (e.g., the even- and odd-parity modes) loses the original degeneracy and orthogonality.<sup>21,22</sup> Consequently, chiral EPs can be readily obtained, paving the way to a plethora of novel and counterintuitive effects ranging from magnetic-free non-reciprocity<sup>23,24</sup> to single-photon blockade,<sup>25</sup> unidirectional emission,<sup>19</sup> and loss-induced revival of lasing<sup>18</sup> to nonlinear sensor responses.<sup>26</sup> Recently, maneuvering of EPs enables control over the local density of states and spontaneous emission dynamics.<sup>27–30</sup> For these established schemes,<sup>15,19,20,31</sup> the inter-modal coupling strength is primarily regulated. However, perturbations may contribute to the far-field radiative channels. In addition, the decay channels might be coherently coupled,<sup>32</sup> known as “external coupling.” Despite the great achievement of non-Hermitian photonics in single WGM microresonators,<sup>1</sup> the interplay between the coexisting internal and external coupling remains rarely explored.<sup>32</sup> Harness-

ing parametric external coupling could open up opportunities in WGM-based phenomena and functionalities.

In this paper, external coupling in single WGM microresonators has been systematically studied. The mode degeneracy becomes broken by introducing a mode-mismatch segment and forming a spiral ring geometry. In addition to the widely investigated inter-modal coupling,<sup>21,33–35</sup> here, the interference of coherent radiation into the far field is tailored by leveraging the geometric parameters, steering the system to a sweet point featuring maximized suppression of decay channels. Such a phenomenon is essentially the same as resonance trapping observed in an open microwave cavity.<sup>36</sup> The subtle transition between external and internal coupling-dominated regimes is revealed using a generalized Hamiltonian model. Furthermore, efficient modulation of emission spectra is experimentally observed using rolled-up microresonators with a spiral-ring-shaped cross-section, featuring great flexibility in tailoring emission dynamics through resonance trapping.

## RESULTS

### Principle

In the widely investigated two-scatterers scheme,<sup>15,19,20</sup> nano-scatterers are placed near the boundary of the resonator, primarily leading to backscattering between counterpropagating waves, and hence constructive or destructive interference of the scattered wave inside the resonator. To harness the regulation of far-field radiative channels for potential external coupling phenomena, here, we introduce a deformed ring structure with an embedded mode-mismatch segment following a spiral geometry (see Figure 1A). Two effective geometric parameters of this segment, namely the length  $d$  and the lateral offset  $T$ , are adjustable. As visualized in the inset, the inner and outer edges act like local scatterers, facilitating backscattering between the clockwise (CW) and counterclockwise (CCW) propagating light

waves, namely internal mode coupling.<sup>37</sup> The backscattering induced by the inner and outer edges may be highly asymmetric, which gives rise to strong mode chirality and, potentially, EPs (see the left panel of Figure 1B). Using a two-mode approximation,<sup>15</sup> for the outer edge, the perturbation Hamiltonian in the standing-wave basis (even mode [1,0]; odd mode [0,1]) can be written as:

$$H_{\text{out}} = \begin{pmatrix} 2\mathbf{V}_e & 0 \\ 0 & 2\mathbf{V}_o \end{pmatrix}, \quad (\text{Equation 1})$$

where the real part of  $\mathbf{V}_e$  ( $\mathbf{V}_o$ ) is the frequency shift of the even (odd) mode (see the left panel of Figure 1B), and the imaginary part is the corresponding change of loss rate. The same analysis of  $\mathbf{H}_{\text{in}}$  applies to the inner edge (see Note S1).

Notably, there is no exact correlation between the imaginary parts of  $\mathbf{V}_e$ ,  $\mathbf{V}_o$ ,  $\mathbf{U}_e$ , and  $\mathbf{U}_o$ , indicating that coherent radiation coupling via the same channel is not considered in this context. In fact, the waveguiding modal mismatch between the regular and widened segments leads to radiation into the far field via mode conversion.<sup>38</sup> Since radiation through identical decay channels would interfere with each other, external coupling emerges as a critical degree of freedom. Similar to Friedrich and Wintgen's theory,<sup>8</sup> the Hamiltonian in the standing wave basis can be written as:

$$H_{\text{ex}} = -i \begin{pmatrix} \gamma_e & e^{i\varphi} \sqrt{\gamma_e \gamma_o} \\ e^{i\varphi} \sqrt{\gamma_e \gamma_o} & \gamma_o \end{pmatrix}, \quad (\text{Equation 2})$$

where  $\gamma_e$  ( $\gamma_o$ ) is the loss rate of the even (odd) mode due to radiation into the far field, and  $\varphi$  is the phase shift between the two radiative components. The interference gives rise to the via-the-continuum coupling term  $e^{i\varphi} \sqrt{\gamma_e \gamma_o}$ , and consequently enhancement or suppression of radiation, as depicted in the right panel of Figure 1B.

Considering both the internal and external coupling effects, the total effective Hamiltonian can be formulated in the traveling-wave basis (CCW (1,0); CW (0,1)) (see Note S1),

$$H = \begin{pmatrix} \mathbf{E} & \mathbf{A} \\ \mathbf{B} & \mathbf{E} \end{pmatrix}, \quad (\text{Equation 3})$$

with

$$\mathbf{E} = E_0 - i\gamma_0 - i\frac{\gamma_e + \gamma_o}{2} + \mathbf{V}_e + \mathbf{V}_o + \mathbf{U}_e + \mathbf{U}_o, \quad (\text{Equation 4})$$

$$\mathbf{A} = \mathbf{V}_e - \mathbf{V}_o + (\mathbf{U}_e - \mathbf{U}_o)e^{-i2m\theta} - i\frac{\gamma_e - \gamma_o}{2} - e^{i\varphi} \sqrt{\gamma_e \gamma_o}, \quad (\text{Equation 5})$$

$$\mathbf{B} = \mathbf{V}_e - \mathbf{V}_o + (\mathbf{U}_e - \mathbf{U}_o)e^{i2m\theta} - i\frac{\gamma_e - \gamma_o}{2} + e^{i\varphi} \sqrt{\gamma_e \gamma_o}, \quad (\text{Equation 6})$$

where  $E_0$  is the original eigenenergy,  $\gamma_0$  is the intrinsic loss of the resonator (e.g., material absorption),  $\theta$  is the relative azimuthal position of two spiral edges, and  $m$  is the azimuthal mode order of the mode pair. Consequently, the eigenvalues can be derived as:  $E_{\pm}(\theta) = E_0 - i\gamma_0 - i\frac{\gamma_e + \gamma_o}{2} + \mathbf{V}_e + \mathbf{V}_o + \mathbf{U}_e + \mathbf{U}_o \pm \sqrt{\mathbf{A}\mathbf{B}}$ .

### Visualizing resonance trapping in parameter space

To elucidate the mechanism of external coupling, a simplified scenario is presented, before delving into a more comprehensive case that incorporates all variables within the non-Hermitian framework (see Note S2). Here, the perturbation-induced losses that do not contribute to external coupling are neglected (i.e., the imaginary parts of  $\mathbf{V}_e$ ,  $\mathbf{V}_o$ ,  $\mathbf{U}_e$ , and  $\mathbf{U}_o$  are zero), while only the radiations via the same channels are considered. Moreover, for spiral-shaped microrings, one can treat two spiral edges as localized defects perturbing the eigenmodes. Here,  $\mathbf{V}_o$  ( $\mathbf{U}_o$ ) could be much smaller than  $\mathbf{V}_e$  ( $\mathbf{U}_e$ ), and we set  $\mathbf{V}_o = \mathbf{U}_o = 0$  for simplicity. Assuming that the two radiative components are balanced (i.e.,  $\gamma_e = \gamma_o = \Gamma$ , where  $\Gamma = \sqrt{\gamma_e \gamma_o}$  is defined as the external coupling strength) and in phase (i.e.,  $e^{i\varphi} = 1$ ), the term  $\sqrt{\mathbf{A}\mathbf{B}}$  in eigenvalues can be written as:

$$\sqrt{\mathbf{A}\mathbf{B}} = \sqrt{V_e^2 + U_e^2 + 2V_e U_e \cos(2m\theta) - \Gamma^2 - 2i\Gamma U_e \sin(2m\theta)}. \quad (\text{Equation 7})$$

According to Equation 7, the eigenvalue surface can be derived in a  $\Gamma$ - $m\theta$  parameter space. As presented in the top panel of Figure 2A, changing  $\theta$  modulates the splitting of eigenenergies  $\delta E = \text{Re}(E_+) - \text{Re}(E_-)$ . The minimized splitting width  $\delta E$  can be reached at  $m\theta = \pi/2$  and eventually becomes zero due to the vanished real part of  $\sqrt{\mathbf{A}\mathbf{B}}$  upon a sufficiently large  $\Gamma$  (i.e.,  $\Gamma > 0.01$  meV). Meanwhile, the imaginary part of eigenvalues  $\text{Im}(E_{\pm})$  is modulated by varying  $m\theta$ . As the lifetime and the Q factor are inversely proportional to  $\text{Im}(E_{\pm})$ , the mode pair can be distinguished into a long-lived mode and a short-lived mode. A clear diverging trend of  $\text{Im}(E_{\pm})$  is observed upon  $m\theta$  approaching  $\pi/2$ , certifying resonance trapping with maximized contrast between Q factors. The contrast of Q factors reduces as  $m\theta$  deviates from  $\pi/2$ . The weakened resonance trapping is attributed to the reinforced inter-modal coupling-induced mode splitting and consequently, the mitigated destructive interference at the far field.

One can track the modulation of Q factors for the mode pair upon varying external coupling strength  $\Gamma$  (see Figure 2B). Upon  $\Gamma = 0.05$  meV, the contrast between the Q factors reaches approximately 33-fold at  $m\theta = \pi/2$ . Upon a decreased  $\Gamma = 0.015$  meV, while the diverging trend of Q factors remains, the discernible approach of Q factors at  $m\theta = \pi/2$  indicates that the system is no longer solely dominated by external coupling. The competition between internal and external coupling leads to compromised resonance trapping. Nevertheless, the two eigenmodes preserve their characteristics as long-lived and short-lived modes, as the “exchange of identity” does not occur upon weak internal coupling.<sup>32</sup> By balancing the strength between internal and external coupling terms, namely  $|V_e - U_e| = \Gamma = 0.01$  meV, coincidence of  $\text{Im}(E_{\pm})$  can be reached at  $m\theta = \pi/2$ . In Figure 2C, the calculated eigenvalue surfaces upon moderate  $\Gamma$  reveal two intersecting Riemann sheets wrapped around the coincidence as an EP, where two eigenvalues coalesce together with their associated eigenvectors. Upon a further decreased  $\Gamma$ , the contrast of Q factors near  $m\theta = \pi/2$  is suppressed further, while crossing of eigenenergies remains, owing to the efficient mode hybridization and the dominance of strong internal coupling.

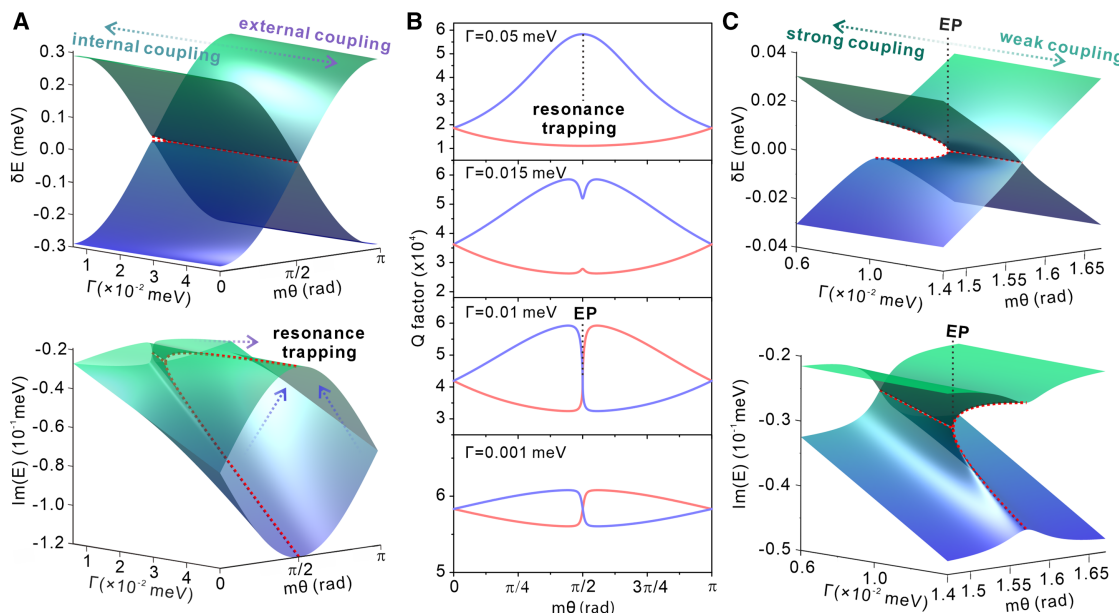


**Figure 2. Evolution of eigenvalues in  $\Gamma$ - $m\theta$  parameter space**

(A) Numerically calculated eigenvalue surfaces in  $\Gamma$ - $m\theta$  parameter space, including  $\delta E$  (top), and  $\text{Im}(E)$  (bottom). We adopted values of  $\gamma_0 = 0.035 \text{ meV}$ ,  $E_0 = 2.638 \text{ eV}$ ,  $\mathbf{V}_e = -0.15 \text{ meV}$ , and  $\mathbf{U}_e = -0.14 \text{ meV}$ . Without losing generality, we set localized perturbations with  $\mathbf{V}_o = \mathbf{U}_o = 0$ . Red dashed lines denote the values upon  $m\theta = \pi/2$ .

(B) Calculated Q factors of the mode pair as a function of  $\theta$  for  $\Gamma$  of 0.05, 0.015, 0.01, and 0.001 meV, respectively.

(C) Magnified view of (A) illustrating the vicinity of an EP within the internal coupling-dominated regime. Red dashed lines denote the values upon  $m\theta = \pi/2$ .

### Parametric external and internal coupling

After introducing the analytical model, we elaborate a practical route of parametric mode coupling, utilizing two geometric parameters,  $T$  and  $\theta$  (effectively determining the length of the mode-mismatch segment). Two-dimensional numerical simulations using the finite-element method were conducted (see methods). Figure 3A summarizes four typical scenarios of mode coupling in the parametric space. In general, the energies of two non-degenerate modes show a linear-like dependence on  $\theta$ . In the regime of external coupling ( $T = 27 \text{ nm}$ ), alongside the crossing of eigenenergies, one can discern a clear diverging trend for Q factors, validating the occurrence of resonance trapping. The slight misalignment between the zero-detuning point ( $\theta \approx 0.367 \text{ rad}$ ) and the optimal resonance trapping ( $\theta \approx 0.361 \text{ rad}$ ) is attributed to the accompanying complexity of radiations (e.g., contributions of other loss sources, or the unbalanced radiation components; see Notes S2 and S3).

Upon resonance trapping, the mode field distributions in Figures 3Bi and 3Bii can be identified as highly regular WGMs. In addition, the majority of the far-field radiation is due to the mode-mismatch segment.<sup>39</sup> One can identify distinct radiation patterns between long- and short-lived modes. The leakage channels can be visualized using the Husimi function.<sup>38</sup> Here, the Husimi projection of both modes presents consistent chirality, with the superiority of the CCW component over the CW component (see Figure 3C). Judging from the distributions inside the leaky region in Figure 3D, resonance trapping renders a substantial reduction of radiation, with  $|\sin(\chi)| \sim 0.3 - 0.6$  at the mode-mismatch segment (i.e., azimuthal angle  $\psi$  between 285° and 317°).

Adjusting the lateral offset of the mode-mismatch segment  $T$  steers the system into the regime of coexisting external and internal coupling. For  $T = 38 \text{ nm}$ , around the zero-detuning point at  $\theta = 0.364 \text{ rad}$ , the Q factors converge, indicating the slight mixing of wave functions via internal coupling. Moreover, the transition point between strong and weak internal coupling, namely EP, can be reached at  $T = 42 \text{ nm}$ , where spectral crossing for both real and imaginary parts can be found at  $\theta = 0.364 \text{ rad}$ . For  $T = 44 \text{ nm}$ , an avoided crossing of branches and a crossing in the Q factors are observed, verifying the nature of strong coupling. Unlike regular WGM patterns in Figures 3Bi and 3Bii, the mode field distributions of the strongly hybridized mode pair reveal a zig-zag-like trajectory in the mode-mismatch segment (see Figures 3Biii and 3Biv), certifying the reinforced inter-modal backscattering between the CW and CCW light wave components. Furthermore, according to the Husimi projection (see Note S4), the strong mode hybridization leads to an elevated mode chirality compared with Figure 3C in the external coupling-dominated regime, which shows consistency with the modeling results in Note S5.

Figure 3E summarizes the parametric mode coupling behavior at the zero-detuning point upon varying  $T$ . Increasing  $T$  efficiently contributes to additional modal mismatch between two segments of the resonator. As a result, the competition between the simultaneously lifted strengths of internal and external coupling eventually reconfigures the non-Hermiticity of the system. Therefore, the scaling parameter  $T$  serves as an intuitive control knob to adjust the primary mode coupling behavior.

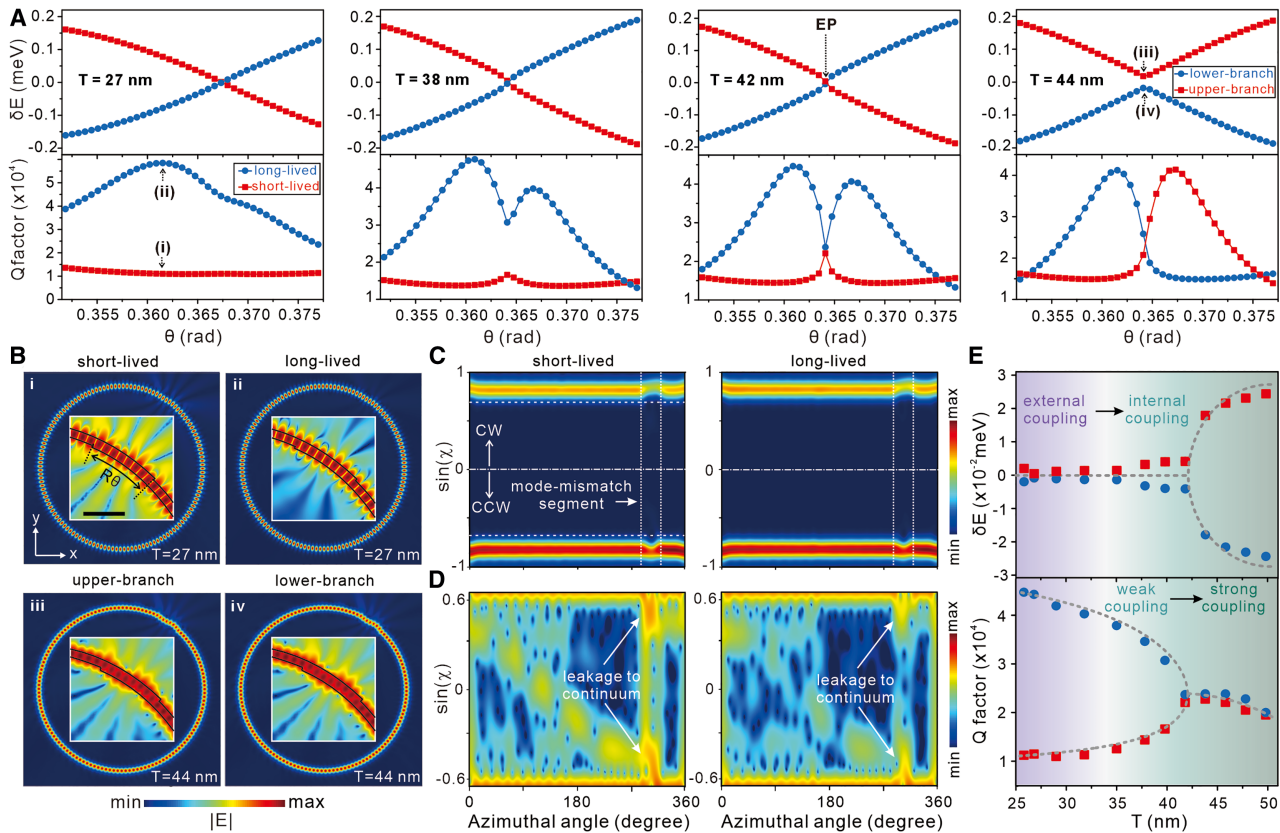


**Figure 3. Parametric external and internal coupling**

(A) Simulated modulation of the mode coupling, including  $\delta E$  (top) and Q factor (bottom).  $W_R$  of 125 nm and  $R$  of 3  $\mu\text{m}$  were fixed.  
(B) Simulated mode field distributions of the mode pair in the external coupling-dominated (i and ii) and strong internal coupling-dominated (iii and iv) regimes. The embedded pictures are enlarged views around the mode-mismatch segment using a logarithmic scale, with a scale bar of 500 nm.  
(C) Extracted internal emerging Husimi functions at the outer boundary of the resonator from the short-lived (left) and long-lived (right) modes. The dashed lines indicate the critical angle for total internal reflection. In this representation, the angle  $\chi$  is defined as negative for CCW components.  
(D) Magnified view of the leaky region in (C) using a logarithmic scale.  
(E) Summarizes the minimized  $\delta E$  (top) and the corresponding Q factors (bottom) as a function of  $T$ . Data were extracted at the point of minimal  $\delta E$ . Gray dashed line: fitted curves using the theoretical model.

#### Tailoring spontaneous emission via resonance trapping

Having established the mechanism of resonance trapping, one can further investigate its physical consequences—specifically, how such a mechanism can be harnessed to tailor the cavity-enhanced light emission. As shown in Figure 4A, an embedded emitter located within the mode volume of the resonator is optically pumped. The excited photoluminescence primarily is coupled to WGMs along both directions. The dynamics can be described using temporal coupled-mode theory<sup>29</sup>:

$$i \frac{d}{dt} \begin{pmatrix} a_{CCW} \\ a_{CW} \end{pmatrix} = \begin{pmatrix} \mathbf{E} & \mathbf{A} \\ \mathbf{B} & \mathbf{E} \end{pmatrix} \begin{pmatrix} a_{CCW} \\ a_{CW} \end{pmatrix} + J \begin{pmatrix} e^{-i\left(\frac{E_e}{\hbar}t+\phi\right)} \\ e^{-i\left(\frac{E_e}{\hbar}t-\phi\right)} \end{pmatrix}, \quad (\text{Equation 8})$$

where  $a_{CCW}$  ( $a_{CW}$ ) represents the amplitude distribution of the CCW (CW) mode,  $J$  is the constant value for optical fields at a

particular transverse position along the propagation direction,  $\hbar$  is the reduced Planck constant, and  $E_e$  represents the emission energy.  $\phi$  denotes the accumulated phase between the localized emitter and the reference point.

By solving Equation 8, we obtain the steady-state field amplitude distributions of the CCW and CW modes:

$$a_{CCW} = \frac{Je^{-i\phi}(E - E_e) - \mathbf{A}Je^{i\phi}}{(E - E_e)^2 - \mathbf{AB}}, \quad (\text{Equation 9})$$

$$a_{CW} = \frac{Je^{i\phi}(E - E_e) - \mathbf{B}Je^{-i\phi}}{(E - E_e)^2 - \mathbf{AB}}. \quad (\text{Equation 10})$$

One can calculate the buildup cavity field intensity using the following equation<sup>23</sup>:

$$I_c(E_e) = |a_{CCW}(E_e)|^2 + |a_{CW}(E_e)|^2. \quad (\text{Equation 11})$$

Figure 4B shows the calculated peak intensity  $I_c(E_e)$  in the  $T$ - $m\theta$  parameter space. In the conventional internal coupling

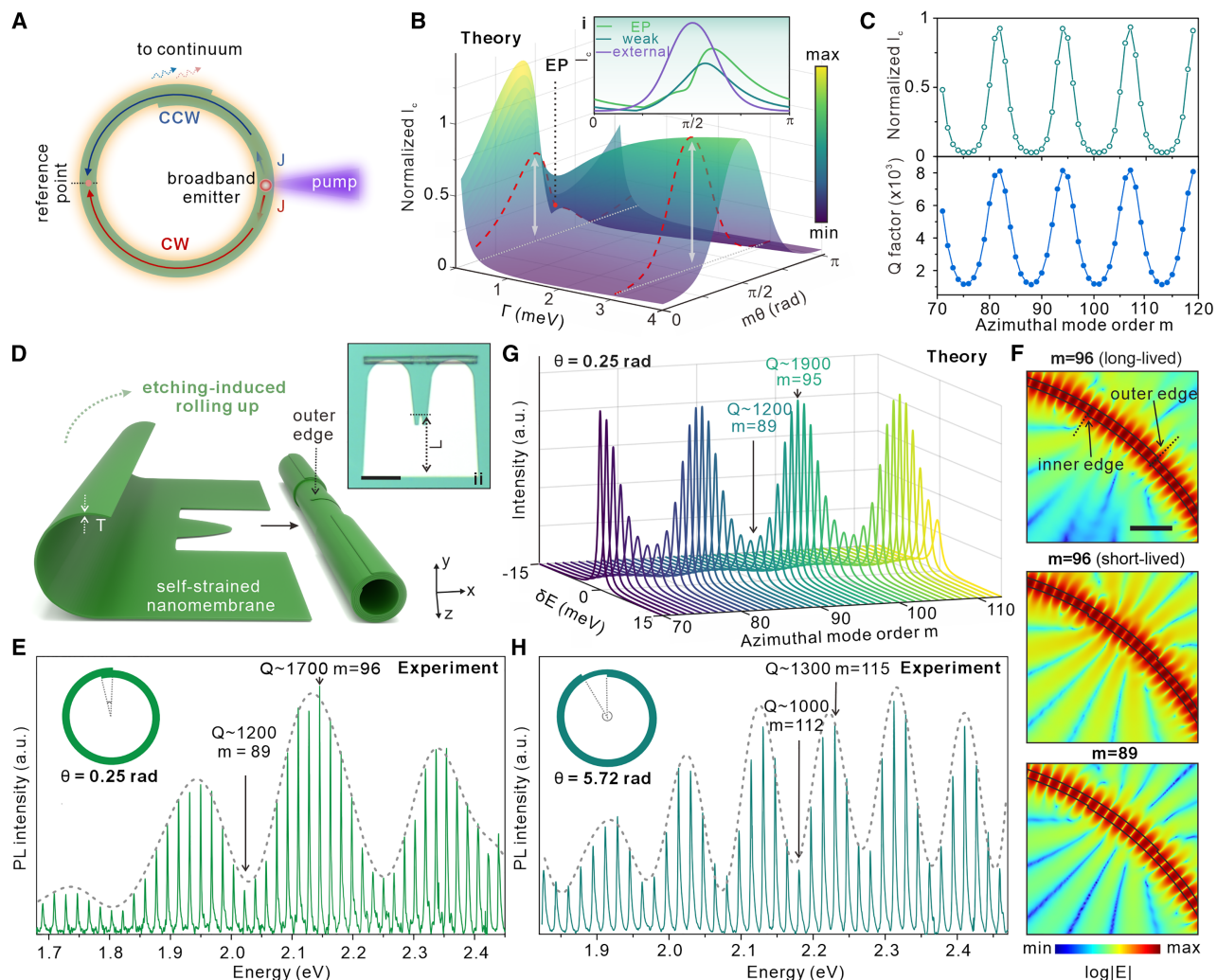


**Figure 4.** Tailored spontaneous emission via resonance trapping

- (A) Schematic of the emitter-resonator system, with the reference point set 180° angular distance to the emitter.
- (B) Numerically calculated surface of the mode normalized peak intensity  $I_c$  as a function of  $\Gamma$  and  $m\theta$ . Here, we set  $V_e = -1.14$  meV,  $U_e = -0.83$  meV, and  $\gamma_0 = 0.1$  meV. Inset i: normalized intensity modulation curves as a function of  $m\theta$  under EP ( $\Gamma = 0.31$  meV), weak coupling ( $\Gamma = 0.53$  meV), and external coupling ( $\Gamma = 3$  meV).
- (C) Numerically calculated normalized  $I_c$  (top) and Q factors (bottom) as functions of azimuthal mode number  $m$ .
- (D) Schematic of a microresonator developed by rolling origami technology. Inset ii: optical microscope image of the microtubular-shaped resonator, with a scale bar of 50  $\mu$ m.
- (E) Measured resonant spectra for a rolled-up microtubular resonator with  $\theta \sim 0.25$  rad, including the sketches of the cross-sectional geometry. Gray dashed line: visual aid.
- (F) Simulated mode field distributions of the mode pairs for a spiral ring with  $\Delta m = 0.25$  rad for  $m = 96$  (top and center) and 89 (bottom), with a scale bar of 500 nm.
- (G) Numerically modeled spectral line shapes for  $m$  between 70 and 113. To fit the experimental results, we set  $V_e = -1.14$  meV,  $U_e = -0.83$  meV,  $\Gamma = 4$  meV, and  $\gamma_0 = 0.45$  meV.
- (H) Measured resonant spectra for a rolled-up microtubular resonator with  $\theta \sim 5.72$  rad, including the sketches of the cross-sectional geometry. The other geometric parameters (e.g.,  $T$ ,  $W_R$ ) are the same as those in (E). Gray dashed line: visual aid.

regime (i.e., small  $\Gamma$ ), the modulation effect on  $I_c(E_e)$  is moderate (with a ratio of 13 under weak coupling, see Figure 4Bi). As the system enters the external coupling regime, the modulation is markedly enhanced, reaching a ratio as high as 35 at  $\Gamma = 3$  meV (see Figure 4B, inset i).

Unlike subwavelength resonators supporting very few modes,<sup>11,40,41</sup> resonance trapping in WGM microresonators applies to its large mode family. Here, we further investigate

the impact of external coupling on broadband emission involving a wide variety of resonant modes with different  $m$  (see methods). Regarding the case of a single dipole emitter, one can refer to Note S6. As revealed in the calculation results in Figure 4C, when setting  $\theta = 0.25$  rad, periodical modulation with a period of  $\Delta m = 12$  is observed, showing consistency with the Q factor of the long-lived mode. The external coupling exhibits mode-dependent Purcell

enhancement,<sup>42</sup> which consequently enables tailored control of the spectral emission profile.<sup>30</sup>

In practice, the proposed spiral microring geometry can be readily obtained through lithography-based approaches.<sup>37</sup> Alternatively, nanomembrane origami technology enables mass fabrication of tubular-shaped microresonators with an inherent spiral-ring-shaped cross-section (see Figure 4D).<sup>38,39,43–46</sup> The precision control on key geometric parameters of the spiral ring, mainly  $T$  (effectively the thickness of the monolayered nanomembrane) and  $\theta$  (determined by the total rolling length  $L$ ), facilitates experimental studies of parametric external coupling.

For a fabricated silica-based microtubular resonator with  $\theta \sim 0.25$  rad operating in the external coupling regime (see Figure 4D, inset ii and methods), the characterized broadband multimode emission with an  $m$  of 71–113 can be observed in the spectrum (see Figure 4E). Clear periodic modulation with period  $\Delta m = 12$  is evident. The discerned modes with a higher peak intensity correspond to larger Q factors (e.g.,  $m = 96$  with  $Q = 1,700$ ).

Numerical simulations of eigenmodes were performed by adopting the same geometric parameters (see Note S7). A consistent periodicity with  $\Delta m = 12$  was observed in the simulated  $\Delta E$  and Q factors, which aligns well with the experimental observations. Optimal resonance trapping at mode order  $m = 96$  (see Figure 4F, top and center panels) produces a 1.8-fold Q factor contrast, yielding distinct far-field radiation patterns between long- and short-lived modes. In contrast, for  $m = 89$  (see Figure 4F, bottom panel), the weakened trapping effect produces comparable and moderate radiation from both modes.

According to the theory, excellent agreement is found with the modeled mode-dependent spectral line shapes in Figure 4G, which again examines the underlying mechanism of Purcell enhancement selectively tailored by resonance trapping. Optimal resonance trapping is achieved while the criterion  $m\theta = \pi/2$  is satisfied. In practice, the winding was adjusted by changing the rolling length  $L$  of the pre-strained nanomembrane pattern, offering a practical route for reshaping the spectra. For another fabricated resonator with  $\theta$  at 5.72 rad (see Figure 4H), periodic modulation was discerned with  $\Delta m = 6$ , which agrees well with the modeling results. Moreover, the resonance trapping was further confirmed in microresonators across different material platforms, highlighting its generality (see Note S8).

## DISCUSSION

External coupling via the continuum, a distinctive concept in non-Hermitian photonics, has been investigated in single WGM optical microresonators with a mode-mismatch segment featuring a broken mode degeneracy. Differing from previous investigations primarily focusing on inter-modal coupling, here, the non-Hermiticity becomes essentially determined by the interplay between internal and external coupling. According to the generalized Hamiltonian model, the geometric parameters of resonators were proposed as intuitive control knobs, driving the system into the regime dominated by external coupling, and achieving resonance trapping with maximized suppression of leakage channels.

As a practical demonstration, three-dimensional (3D) nanomembrane-based microtube cavities with inherent spiral-shaped cross-sections have been experimentally studied. Observations of modulated broadband multimode emission spectra affirm the existence of mode-dependent resonance trapping. All in all, the elucidated mechanism of external coupling via the continuum in single asymmetric WGM microresonators is envisaged to offer a pathway to emerging functionalities in integrable devices, particularly nonlinear frequency conversion,<sup>47</sup> mode-selective emission,<sup>43,48,49</sup> and structured light generation.<sup>50</sup>

## METHODS

### Numerical simulations

Two-dimensional simulations of optical resonant modes in spiral-shaped microring resonators were conducted using the finite-element method (COMSOL Multiphysics 5.6 wave-optics module). A circular-shaped perfect matching layer as the outermost boundary was introduced. The effective refractive index  $n_{\text{eff}}$  of the multilayered ring resonator was set to 1.95/1.48/1.95 ( $\text{HfO}_2/\text{SiO}_x/\text{HfO}_2$ ). To mimic the resonator samples characterized in the experiments, the nonradiative damping and the surface roughness-induced scattering were considered in the imaginary part of  $n_{\text{eff}}$  ( $4 \times 10^{-5} \text{ i}$ ) of the nanomembrane layers. The fine-meshing condition was applied to the cavity region with a grid size of <20 nm. Pairs of nearly degenerate, transverse-magnetic (TM, defined as the electric field parallel to the z axis) polarized eigenmodes, and their associated eigenenergies were calculated using the eigenmode solver. The internal emerging Husimi function was calculated following our previous methods using the simulated electric fields of the mode pair as inputs.<sup>38</sup>

### Device fabrication

Nanomembrane-based optical microtube cavities were fabricated mainly based on our developed process described in our earlier work.<sup>38</sup> Key geometric parameters, such as  $R$ ,  $W_R$ ,  $T$ , and  $\theta$ , were precisely controlled through a nanomembrane origami approach.<sup>51</sup> The process began with patterning a photoresist layer (ARP-3510, Allresists GmbH) on a silicon substrate covered by a 1-μm-thick thermal oxide layer using maskless lithography (μPG 101, Heidelberg Instruments). To enhance axial confinement, a lobe-shaped design was incorporated at the center of the nanomembrane pattern, forming an optical quasi-potential well (see Figure 4A).<sup>52</sup> Next, layers of 10-nm SiO and 30-nm  $\text{SiO}_2$ , were deposited via angled electron-beam deposition (Auto500 e-beam, Edwards Vacuum) at an incident angle of 60°. The deposition rates (5 Å/s for SiO and 0.5 Å/s for  $\text{SiO}_2$ ) were carefully controlled to achieve the desired strain levels, facilitating the subsequent rolling process. Rolling was triggered by dissolving the photoresist in dimethyl sulfoxide. A critical point dryer (931 GL, Tousimis CPD) was employed to maintain structural integrity during solvent evaporation. Lastly, a 20-nm-thick  $\text{HfO}_2$  layer was deposited on the microtube surface using atomic layer deposition (FLEXAL, Oxford Instruments) to improve optical confinement. The mismatch segment and edges of the fabricated microtube are clearly visible, as shown in the scanning electron microscopy image in Note S9.

## Sample characterizations

Resonant spectra were recorded using a confocal photoluminescence system (LabRAM HR Evolution, HORIBA Scientific) (see Note S9). A continuous-wave laser beam (Cobolt Twist, 457 nm) was used to excite broadband emission through a long working distance objective lens (Olympus LMPLFLN 50 × , numerical aperture 0.5) with a spot size of approximately  $1 \mu\text{m}^2$ . Broadband photoluminescence ( $\sim 1.7\text{--}2.4 \text{ eV}$ ), generated by defects in the  $\text{SiO}/\text{SiO}_2$  nanomembrane, predominantly coupled into the WGM resonances. The resonance signals were collected via the same objective lens, filtered using a polarization analyzer (selecting TM modes with the electric field aligned to the tube axis z), and analyzed by a spectrometer with a  $600\text{-blz/mm}^{-1}$  grating.

## RESOURCE AVAILABILITY

### Lead contact

Requests for further information and resources should be directed to and will be fulfilled by the lead contact, Jiawei Wang ([wangjw7@hit.edu.cn](mailto:wangjw7@hit.edu.cn)).

### Materials availability

This study did not generate new materials.

### Data and code availability

The published article includes all data analyzed during this study. Any additional information required to reanalyze the data reported in this paper is available from the [lead contact](#) upon request.

## ACKNOWLEDGMENTS

J.W. acknowledges support from the National Natural Science Foundation of China under grant nos. 62422503, 12474375, and 62305093; the Guangdong Basic and Applied Basic Research Foundation Regional Joint Fund under grant no. 2023A1515011944; and the Science and Technology Innovation Commission of Shenzhen under grant nos. JCYJ20220531095604009 and RCYX20221008092907027. M.T. and L.M. acknowledge financial support from the Würzburg-Dresden Cluster of Excellence on Complexity and Topology in Quantum Matter—ct. qmat (EXC 2147, project ID 390858490) and the German Research Foundation (grant no. MA 7968/2-1).

## AUTHOR CONTRIBUTIONS

Conceptualization: J.W. and L.M. Theoretical analysis: J.L. and M.T. Investigation: J.L., M.T., X.W., and C.N.S. Data analysis: J.W., J.L., and Q.S. Writing – original draft: J.L., J.W., and O.G.S. Writing – review & editing: all authors. Resources: X.W. and C.N.S. Supervision: J.W.

## DECLARATION OF INTERESTS

The authors declare no competing interests.

## SUPPLEMENTAL INFORMATION

Supplemental information can be found online at <https://doi.org/10.1016/j.newton.2025.100171>.

Received: January 2, 2025

Revised: April 23, 2025

Accepted: June 17, 2025

Published: July 14, 2025

## REFERENCES

- Wang, C., Fu, Z., Mao, W., Qie, J., Stone, A.D., and Yang, L. (2023). Non-Hermitian optics and photonics: from classical to quantum. *Adv. Opt. Photonics* 15, 442. <https://doi.org/10.1364/AOP.475477>.
- Ozdemir, S.K., Rotter, S., Nori, F., and Yang, L. (2019). Parity-time symmetry and exceptional points in photonics. *Nat. Mater.* 18, 783–798. <https://doi.org/10.1038/s41563-019-0304-9>.
- Li, A., Wei, H., Cotrufo, M., Chen, W., Mann, S., Ni, X., Xu, B., Chen, J., Wang, J., Fan, S., et al. (2023). Exceptional points and non-Hermitian photonics at the nanoscale. *Nat. Nanotechnol.* 18, 706–720. <https://doi.org/10.1038/s41565-023-01408-0>.
- Miri, M.A., and Alù, A. (2019). Exceptional points in optics and photonics. *Science* 363, aar7709. <https://doi.org/10.1126/science.aar7709>.
- Marinica, D.C., Borisov, A.G., and Shabanov, S.V. (2008). Bound states in the continuum in photonics. *Phys. Rev. Lett.* 100, 183902. <https://doi.org/10.1103/PhysRevLett.100.183902>.
- Chen, W., Chen, Y., and Liu, W. (2019). Multipolar conversion induced subwavelength high-Q Kerker supermodes with unidirectional radiations. *Laser Photon. Rev.* 13, 1900067. <https://doi.org/10.1002/lpor.201900067>.
- Rybin, M.V., Koshelev, K.L., Sadrieva, Z.F., Samusev, K.B., Bogdanov, A., Limonov, M.F., and Kivshar, Y.S. (2017). High-Q supercavity modes in subwavelength dielectric resonators. *Phys. Rev. Lett.* 119, 243901. <https://doi.org/10.1103/PhysRevLett.119.243901>.
- Hsu, C.W., Zhen, B., Stone, A.D., Joannopoulos, J.D., and Soljačić, M. (2016). Bound states in the continuum. *Nat. Rev. Mater.* 1, 16048. <https://doi.org/10.1038/natrevmats.2016.48>.
- Tang, H., Wang, Y., Chen, Y., Wang, K., He, X., Huang, C., Xiao, S., Yu, S., and Song, Q. (2023). Ultrahigh-Q lead halide perovskite microlasers. *Nano Lett.* 23, 3418–3425. <https://doi.org/10.1021/acs.nanolett.3c00463>.
- Wiersig, J. (2006). Formation of long-lived, scarlike modes near avoided resonance crossings in optical microcavities. *Phys. Rev. Lett.* 97, 253901. <https://doi.org/10.1103/PhysRevLett.97.253901>.
- Riabov, D., Gladkov, R., Pashina, O., Bogdanov, A., and Makarov, S. (2024). Subwavelength Raman laser driven by quasi bound state in the continuum. *Laser Photon. Rev.* 18, 2300829. <https://doi.org/10.1002/lpor.202300829>.
- Friedrich, H., and Wintgen, D. (1985). Interfering resonances and bound states in the continuum. *Phys. Rev. A* 32, 3231–3242. <https://doi.org/10.1103/PhysRevA.32.3231>.
- Hodaei, H., Miri, M.A., Heinrich, M., Christodoulides, D.N., and Khajavikhan, M. (2014). Parity-time-symmetric microring lasers. *Science* 346, 975–978. <https://doi.org/10.1126/science.1258480>.
- Lafalce, E., Zeng, Q., Lin, C.H., Smith, M.J., Malak, S.T., Jung, J., Yoon, Y.-J., Lin, Z., Tsukruk, V.V., and Vardeny, Z.V. (2019). Robust lasing modes in coupled colloidal quantum dot microdisk pairs using a non-Hermitian exceptional point. *Nat. Commun.* 10, 561. <https://doi.org/10.1038/s41467-019-08432-6>.
- Wiersig, J. (2011). Structure of whispering-gallery modes in optical microdisks perturbed by nanoparticles. *Phys. Rev. A* 84, 063828. <https://doi.org/10.1103/PhysRevA.84.063828>.
- Wiersig, J. (2014). Enhancing the sensitivity of frequency and energy splitting detection by using exceptional points: application to microcavity sensors for single-particle detection. *Phys. Rev. Lett.* 112, 203901. <https://doi.org/10.1103/PhysRevLett.112.203901>.
- Gwak, S., Kim, H., Yu, H.H., Ryu, J., Kim, C.M., and Yi, C.H. (2021). Rayleigh scatterer-induced steady exceptional points of stable-island modes in a deformed optical microdisk. *Opt. Lett.* 46, 2980–2983. <https://doi.org/10.1364/OL.426470>.
- Peng, B., Özdemir, S.K., Rotter, S., Yilmaz, H., Liertzer, M., Monifi, F., Bender, C.M., Nori, F., and Yang, L. (2014). Loss-induced suppression and revival of lasing. *Science* 346, 328–332. <https://doi.org/10.1126/science.1258004>.

19. Peng, B., Özdemir, S.K., Lierter, M., Chen, W., Kramer, J., Yilmaz, H., Wiersig, J., Rotter, S., and Yang, L. (2016). Chiral modes and directional lasing at exceptional points. *Proc. Natl. Acad. Sci. USA* **113**, 6845–6850. <https://doi.org/10.1073/pnas.1603318113>.
20. Lee, H., Kecebas, A., Wang, F., Chang, L., Özdemir, S.K., and Gu, T. (2023). Chiral exceptional point and coherent suppression of backscattering in silicon microring with low loss Mie scatterer. *eLight* **3**, 20. <https://doi.org/10.1186/s43593-023-00043-5>.
21. Wiersig, J., Kim, S.W., and Hentschel, M. (2008). Asymmetric scattering and nonorthogonal mode patterns in optical microspirals. *Phys. Rev. A* **78**, 053809. <https://doi.org/10.1103/PhysRevA.78.053809>.
22. Yang, J., Shi, S., Yan, S., Zhu, R., Zhao, X., Qin, Y., Fu, B., Chen, X., Li, H., Zuo, Z., et al. (2024). Non-orthogonal cavity modes near exceptional points in the far field. *Commun. Phys.* **7**, 13. <https://doi.org/10.1038/s42005-023-01508-2>.
23. Qie, J., Wang, C., and Yang, L. (2023). Chirality induced nonreciprocity in a nonlinear optical microresonator. *Laser Photon. Rev.* **17**, 2200717. <https://doi.org/10.1002/lpor.202200717>.
24. Muñoz de las Heras, A., Franchi, R., Biasi, S., Ghulinyan, M., Pavese, L., and Carusotto, I. (2021). Nonlinearity-induced reciprocity breaking in a single nonmagnetic taiji resonator. *Phys. Rev. Appl.* **15**, 054044. <https://doi.org/10.1103/PhysRevApplied.15.054044>.
25. Huang, R., Özdemir, J.K., Liao, J., Minganti, F., Kuang, L., Nori, F., and Jing, H. (2022). Exceptional photon blockade: engineering photon blockade with chiral exceptional points. *Laser Photon. Rev.* **16**, 2100430. <https://doi.org/10.1002/lpor.202100430>.
26. Lai, Y.H., Lu, Y.K., Suh, M.G., Yuan, Z., and Vahala, K. (2019). Observation of the exceptional-point-enhanced sagnac effect. *Nature* **576**, 65–69. <https://doi.org/10.1038/s41586-019-1777-z>.
27. Kippenberg, T.J., Tchebotareva, A.L., Kalkman, J., Polman, A., and Vahala, K.J. (2009). Purcell-factor-enhanced scattering from Si nanocrystals in an optical microcavity. *Phys. Rev. Lett.* **103**, 027406. <https://doi.org/10.1103/PhysRevLett.103.027406>.
28. Hashemi, A., Busch, K., Christodoulides, D.N., Özdemir, S.K., and El-Ganainy, R. (2022). Linear response theory of open systems with exceptional points. *Nat. Commun.* **13**, 3281. <https://doi.org/10.1038/s41467-022-30715-8>.
29. Zhong, Q., Hashemi, A., Özdemir, i.m.c.K., and El-Ganainy, R. (2021). Control of spontaneous emission dynamics in microcavities with chiral exceptional surfaces. *Phys. Rev. Res.* **3**, 013220. <https://doi.org/10.1103/PhysRevResearch.3.013220>.
30. Lu, Y., Zhao, Y., Li, R., and Liu, J. (2022). Anomalous spontaneous emission dynamics at chiral exceptional points. *Opt. Express* **30**, 41784–41803. <https://doi.org/10.1364/OE.473824>.
31. Li, J., Tang, M., Duan, J., Xu, X., Xu, K., Ma, L., and Wang, J. (2023). Exceptional points in a spiral ring cavity for enhanced biosensing. *J. Lightwave Technol.* **41**, 1–9. <https://doi.org/10.1109/jlt.2023.3237748>.
32. Cao, H., and Wiersig, J. (2015). Dielectric microcavities: Model systems for wave chaos and non-Hermitian physics. *Rev. Mod. Phys.* **87**, 61–111. <https://doi.org/10.1103/RevModPhys.87.61>.
33. Wang, X., Wang, Z., Dong, H., Saggau, C.N., Tang, H., Tang, M., Liu, L., Baunack, S., Bai, L., Liu, J., et al. (2022). Collective coupling of 3d confined optical modes in monolithic twin microtube cavities formed by nanomembrane origami. *Nano Lett.* **22**, 6692–6699. <https://doi.org/10.1021/acs.nanolett.2c02083>.
34. Wang, J., Yin, Y., Hao, Q., Yang, Y.D., Valligatla, S., Saei Ghareh Naz, E., Li, Y., Saggau, C.N., Ma, L., and Schmidt, O.G. (2018). Curved nanomembrane-based concentric ring cavities for supermode hybridization. *Nano Lett.* **18**, 7261–7267. <https://doi.org/10.1038/s41566-022-01107-7>.
35. Fang, Y., Li, S., and Mei, Y. (2016). Modulation of high quality factors in rolled-up microcavities. *Phys. Rev. A* **94**, 033804. <https://doi.org/10.1103/PhysRevA.94.033804>.
36. Persson, E., Rotter, I., Stöckmann, H.J., and Barth, M. (2000). Observation of resonance trapping in an open microwave cavity. *Phys. Rev. Lett.* **85**, 2478–2481. <https://doi.org/10.1103/PhysRevLett.85.2478>.
37. Chen, Y., Li, J., Xu, K., Biasi, S., Franchi, R., Huang, C., Duan, J., Wang, X., Pavese, L., Xu, X., and Wang, J. (2024). Electrically reconfigurable mode chirality in integrated microring resonators. *Laser Photon. Rev.* **18**, 2301289. <https://doi.org/10.1002/lpor.202301289>.
38. Wang, J., Yin, Y., Yang, Y.D., Hao, Q., Tang, M., Wang, X., Saggau, C.N., Karnaushenko, D., Yan, X., Huang, Y.Z., et al. (2019). Deterministic yet flexible directional light emission from spiral nanomembrane cavities. *ACS Photonics* **6**, 2537–2544. <https://doi.org/10.1021/acspophotonics.9b00992>.
39. Wang, J., Tang, M., Yang, Y.D., Yin, Y., Chen, Y., Saggau, C.N., Zhu, M., Yuan, X., Karnaushenko, D., Huang, Y.Z., et al. (2020). Steering directional light emission and mode chirality through postshaping of cavity geometry. *Laser Photon. Rev.* **14**, 2000118. <https://doi.org/10.1002/lpor.202000118>.
40. Song, Q.H., and Cao, H. (2010). Improving optical confinement in nanostructures via external mode coupling. *Phys. Rev. Lett.* **105**, 053902. <https://doi.org/10.1103/PhysRevLett.105.053902>.
41. Solodovchenko, N., Samusev, K., Bochek, D., and Limonov, M. (2021). Bound states in the continuum in strong-coupling and weak-coupling regimes under the cylinder – ring transition. *Nanophotonics* **10**, 4347–4355. <https://doi.org/10.1515/nanoph-2021-0351>.
42. Chien, C.H., Wu, S.H., Ngo, T.H.B., and Chang, Y.C. (2019). Interplay of Purcell effect, stimulated emission, and leaky modes in the photoluminescence spectra of microsphere cavities. *Phys. Rev. Appl.* **11**, 051001. <https://doi.org/10.1103/PhysRevApplied.11.051001>.
43. Dong, H., Saggau, C.N., Zhu, M., Liang, J., Duan, S., Wang, X., Tang, H., Yin, Y., Wang, X., Wang, J., et al. (2021). Perovskite origami for programmable microtube lasing. *Adv. Funct. Mater.* **31**, 2109080. <https://doi.org/10.1002/adfm.202109080>.
44. Dastjerdi, M.H.T., Djavid, M., and Mi, Z. (2015). An electrically injected rolled-up semiconductor tube laser. *Appl. Phys. Lett.* **106**, 021114. <https://doi.org/10.1002/adma.202003252>.
45. Li, Y., Feng, L., Su, X., Li, Q., Yun, F., Yuan, G., and Han, J. (2017). Whispering gallery mode lasing from InGaN/GaN quantum well microtube. *Opt. Express* **25**, 18072–18080. <https://doi.org/10.1364/OE.25.018072>.
46. Lin, X., Fang, Y., Zhu, L., Zhang, J., Huang, G., Wang, J., and Mei, Y. (2016). Self-rolling of oxide nanomembranes and resonance coupling in tubular optical microcavity. *Adv. Opt. Mater.* **4**, 936–942. <https://doi.org/10.1002/adom.201500776>.
47. Hou, J., Lin, J., Zhu, J., Zhao, G., Chen, Y., Zhang, F., Zheng, Y., Chen, X., Cheng, Y., Ge, L., and Wan, W. (2022). Self-induced transparency in a perfectly absorbing chiral second-harmonic generator. *PhotonIX* **3**, 22. <https://doi.org/10.1186/s43074-022-00068-y>.
48. Tang, L., Tang, J., Zhang, W., Lu, G., Zhang, H., Zhang, Y., Xia, K., and Xiao, M. (2019). On-chip chiral single-photon interface: Isolation and unidirectional emission. *Phys. Rev. A* **99**, 043833. <https://doi.org/10.1103/PhysRevA.99.043833>.
49. Jiang, X., Zou, C., Wang, L., Gong, Q., and Xiao, Y. (2016). Whispering-gallery microcavities with unidirectional laser emission. *Laser Photon. Rev.* **10**, 40–61. <https://doi.org/10.1002/lpor.201500163>.
50. Huang, C., Zhang, C., Xiao, S., Wang, Y., Fan, Y., Liu, Y., Zhang, N., Qu, G., Ji, H., Han, J., et al. (2020). Ultrafast control of vortex microlasers. *Science* **367**, 1018–1021. <https://doi.org/10.1126/science.aba4597>.
51. Saggau, C.N., Gabler, F., Karnaushenko, D.D., Karnaushenko, D., Ma, L., and Schmidt, O.G. (2020). Wafer-scale high-quality microtubular devices fabricated via dry-etching for optical and microelectronic applications. *Adv. Mater.* **32**, 2003252. <https://doi.org/10.1002/adma.202003252>.
52. Strelow, C., Schultz, C.M., Rehberg, H., Sauer, M., Welsch, H., Stemmann, A., Heyn, C., Heitmann, D., and Kipp, T. (2012). Light confinement and mode splitting in rolled-up semiconductor microtube bottle resonators. *Phys. Rev. B* **85**, 155329. <https://doi.org/10.1103/PhysRevB.85.155329>.

**NEWTON, Volume 1**

**Supplemental information**

**Reconfigurable resonance trapping  
in single optical microresonators**

**Jin Li, Min Tang, Xiaoyu Wang, Christian N. Saggau, Yin Yin, Libo Ma, Qinghai Song, Oliver G. Schmidt, and Jiawei Wang**

**This file includes:**

Figures S1-S11.

Note S1: Theoretical model.

Note S2: Contributions of random dissipative coupling.

Note S3: Impact of mismatch between two radiation components.

Note S4: Husimi projections for different coupling regimes.

Note S5: Evolution of mode chirality across different coupling regimes.

Note S6: Supplemental analysis on the emitter-resonator system.

Note S7: Mode-dependent resonance trapping.

Note S8: Supplemental experimental results in alternative material platforms.

Note S9: Supplemental details on sample inspection and experimental setup.

### Note S1: Theoretical model

To analyze a whispering-gallery-mode (WGM) optical microcavity with a lifted degeneracy, the effective Hamiltonian can be described as a two-by-two matrix:

$$H = \begin{pmatrix} \mathbf{E} & \mathbf{A} \\ \mathbf{B} & \mathbf{E} \end{pmatrix}. \quad (\text{S1})$$

The complex-valued diagonal elements  $\mathbf{E}$  describe the original energies of the non-degenerate mode pair with the same azimuthal mode number. In the general non-Hermitian case  $\mathbf{A} \neq \mathbf{B}^*$ , both internal coupling and external coupling via the continuum may occur, and contribute to these two complex-valued off-diagonal elements.

Considering the spiral-shaped microring as one kind of deformed WGM microcavities, the perturbation can be analyzed following the assumption of the previously reported two-mode approximation<sup>5</sup>. The perturbation Hamiltonian of the outer edge in the standing-wave basis [even mode, (1,0); odd mode, (0,1)] can be written as:

$$H_{\text{out}} = \begin{pmatrix} 2\mathbf{V}_e & 0 \\ 0 & 2\mathbf{V}_o \end{pmatrix}, \quad (\text{S2})$$

where the real parts of  $\mathbf{V}_e$  ( $\mathbf{V}_o$ ) are the frequency shift of the even (odd) mode, and the imaginary parts are the corresponding change in the loss rate. Similarly, the perturbation Hamiltonian of the inner edge is

$$H_{\text{in}} = \begin{pmatrix} 2\mathbf{U}_e & 0 \\ 0 & 2\mathbf{U}_o \end{pmatrix}. \quad (\text{S3})$$

Due to the mismatched lateral dimension in the mode-mismatch segment, the resonant mode may be coupled into the far field. The corresponding Hamiltonian can be written as:

$$H_{\text{ex}} = -i \begin{pmatrix} \gamma_e & e^{i\varphi} \sqrt{\gamma_e \gamma_o} \\ e^{i\varphi} \sqrt{\gamma_e \gamma_o} & \gamma_o \end{pmatrix}, \quad (\text{S4})$$

where  $\gamma_e$  ( $\gamma_o$ ) is the loss rate of the even (odd) mode coupled via the continuum, and  $\varphi$  is the phase shift between the two radiative components. In particular, the two resonance modes may share the same radiation channel, and hence, interference of radiation gives rise to the via-the-continuum coupling term  $e^{i\varphi} \sqrt{\gamma_e \gamma_o}$ .

For Hamiltonians described under the standing-wave basis, one can map them to those under the traveling-wave basis. The states reveal definite propagation directions with angular dependence  $\exp(im\phi) = \cos(m\phi)+i\cdot\sin(m\phi)$  (counter-clockwise, CCW) and  $\exp(-im\phi) = \cos(m\phi)-i\cdot\sin(m\phi)$  (clockwise, CW), where  $m$  is the azimuthal mode number, and  $\phi$  is the azimuthal angle. Hence, the transformation matrix can be written as:

$$M^\dagger = \begin{pmatrix} \frac{1}{\sqrt{2}} & -\frac{i}{\sqrt{2}} \\ \frac{1}{\sqrt{2}} & \frac{i}{\sqrt{2}} \end{pmatrix}. \quad (\text{S5})$$

The perturbation of the outer edge in the traveling-wave basis [CCW, (1,0); CW, (0,1)] can be written as:

$$H_{\text{out}} = M^\dagger HM = \begin{pmatrix} \mathbf{V}_e + \mathbf{V}_o & \mathbf{V}_e - \mathbf{V}_o \\ \mathbf{V}_e - \mathbf{V}_o & \mathbf{V}_e + \mathbf{V}_o \end{pmatrix}. \quad (\text{S6})$$

This transformation also applies to the inner edge which is located at a relative angular distance  $\theta$ ,

$$H_{\text{in}} = \begin{pmatrix} \mathbf{U}_e + \mathbf{U}_o & (\mathbf{U}_e - \mathbf{U}_o)e^{-i2m\theta} \\ (\mathbf{U}_e - \mathbf{U}_o)e^{i2m\theta} & \mathbf{U}_e + \mathbf{U}_o \end{pmatrix}. \quad (\text{S7})$$

Equation S4 can be written under the traveling-wave basis as:

$$H_{\text{ex}} = -i \begin{pmatrix} \frac{\gamma_e + \gamma_o}{2} & \frac{\gamma_e - \gamma_o}{2} - ie^{i\varphi} \sqrt{\gamma_e \gamma_o} \\ \frac{\gamma_e - \gamma_o}{2} + ie^{i\varphi} \sqrt{\gamma_e \gamma_o} & \frac{\gamma_e + \gamma_o}{2} \end{pmatrix}. \quad (\text{S8})$$

Hence, the overall Hamiltonian can be expressed as:

$$H = H_0 + H_{\text{in}} + H_{\text{out}} + H_{\text{ex}} + H_{\text{imp}} = \begin{pmatrix} \mathbf{E} & \mathbf{A} \\ \mathbf{B} & \mathbf{E} \end{pmatrix}, \quad (\text{S9})$$

where  $H_0 = \begin{pmatrix} E_0 - i\gamma_0 & 0 \\ 0 & E_0 - i\gamma_0 \end{pmatrix}$  describes the unperturbed eigenmodes,  $E_0$  is the intrinsic resonance energy, and  $\gamma_0$  is the intrinsic loss of the cavity, and  $H_{\text{imp}} = \begin{pmatrix} 0 & \tilde{\varepsilon}_{\text{imp}} \\ \varepsilon_{\text{imp}} & 0 \end{pmatrix}$  quantifies the backscattering introduced by fabrication imperfections. For simplicity, we ignore the minor yet random perturbation caused by fabrication imperfections (i.e.,  $\varepsilon_{\text{imp}} = \tilde{\varepsilon}_{\text{imp}} = 0$ ). The elements in equation S9 become:

$$\mathbf{E} = E_0 - i\gamma_0 - i\frac{\gamma_e + \gamma_o}{2} + \mathbf{V}_e + \mathbf{V}_o + \mathbf{U}_e + \mathbf{U}_o, \quad (\text{S10})$$

$$\mathbf{A} = \mathbf{V}_e - \mathbf{V}_o + (\mathbf{U}_e - \mathbf{U}_o)e^{-i2m\theta} - i\frac{\gamma_e - \gamma_o}{2} - e^{i\varphi}\sqrt{\gamma_e\gamma_o}, \quad (\text{S11})$$

$$\mathbf{B} = \mathbf{V}_e - \mathbf{V}_o + (\mathbf{U}_e - \mathbf{U}_o)e^{i2m\theta} - i\frac{\gamma_e - \gamma_o}{2} + e^{i\varphi}\sqrt{\gamma_e\gamma_o}. \quad (\text{S12})$$

The eigenvalues can be described as:

$$E_{\pm}(\theta) = E_0 - i\gamma_0 - i\frac{\gamma_e + \gamma_o}{2} + \mathbf{V}_e + \mathbf{V}_o + \mathbf{U}_e + \mathbf{U}_o \pm \sqrt{\mathbf{AB}}, \quad (\text{S13})$$

with

$$\sqrt{\mathbf{AB}} = \sqrt{\frac{\Lambda_1^2 + \Lambda_2^2 + 2\Lambda_1\Lambda_2 \cos(2m\theta) - e^{2i\varphi}\Gamma^2}{-2ie^{i\varphi}\Gamma\Lambda_2 \sin(2m\theta) + 2\Delta\Gamma\Lambda_1 + 2\Delta\Gamma\Lambda_2 \cos(2m\theta) + \Delta\Gamma^2}}, \quad (\text{S14})$$

$$\text{where } \Gamma = \sqrt{\gamma_e\gamma_o}, \Delta\Gamma = -i\frac{\gamma_e - \gamma_o}{2}, \Lambda_1 = \mathbf{V}_e - \mathbf{V}_o, \Lambda_2 = \mathbf{U}_e - \mathbf{U}_o.$$

For spiral-shaped microring resonators, one can treat two spiral edges as localized nanoscatterers perturbing the eigenmodes. Hence,  $\mathbf{V}_o$  ( $\mathbf{U}_o$ ) could be much smaller than  $\mathbf{V}_e$  ( $\mathbf{U}_e$ ). Besides,  $\mathbf{V}_e$  ( $\mathbf{U}_e$ ) can be numerically calculated using the dipole approximation<sup>7</sup>. The real part  $\text{Re}(\mathbf{V}_e)$  ( $\text{Re}(\mathbf{U}_e)$ ) represents the contribution to the spectral shift<sup>7</sup>, while the imaginary part  $\text{Im}(\mathbf{V}_e)$  ( $\text{Im}(\mathbf{U}_e)$ ) represents its contribution to the damping rate (corresponding to a negative value). Given the absence of lossy materials (e.g., metals) in the system, we assume that the amplitude of  $\text{Re}(\mathbf{V}_e)$  ( $\text{Re}(\mathbf{U}_e)$ ) is much larger than that of  $\text{Im}(\mathbf{V}_e)$  ( $\text{Im}(\mathbf{U}_e)$ ). By setting  $\mathbf{V}_o = \mathbf{U}_o = 0$ , the equation S14 can be written as follows:

$$\sqrt{\mathbf{AB}} = \sqrt{\frac{\mathbf{V}_e^2 + \mathbf{U}_e^2 + 2\mathbf{V}_e\mathbf{U}_e \cos(2m\theta) - e^{2i\varphi}\Gamma^2}{2ie^{i\varphi}\Gamma\mathbf{U}_e \sin(2m\theta) + 2\Delta\Gamma\mathbf{V}_e + 2\Delta\Gamma\mathbf{U}_e \cos(2m\theta) + \Delta\Gamma^2}}, \quad (\text{S15})$$

$$\text{where } \Gamma = \sqrt{\gamma_e\gamma_o}, \Delta\Gamma = -i\frac{\gamma_e - \gamma_o}{2}.$$

For calculated eigenvalues in equation S15, the imaginary part of the two eigenvalues  $\text{Im}(E_{\pm})$  could be distinct. The quality (Q) factor is defined as  $Q_{\pm} = -\text{Re}(E_{\pm}) / 2\text{Im}(E_{\pm})$ . We term the one with a smaller imaginary part (higher Q) as the “long-lived” mode, and the other one with a larger imaginary part (lower Q) as the “short-lived” mode.

Here we elaborate on defining the regimes dominated by external and internal coupling. The modeling results upon  $\Gamma = 0.05$  meV and  $0.015$  meV are shown in Figure S1 as two examples. Their dominance is distinguished by the sign of the second derivative of

$$Q_{\text{long-lived}}(\theta), \text{ namely } Q_{\text{long-lived}}''(\theta) = \frac{d^2(Q_{\text{long-lived}})}{d\theta^2} \text{ at } m\theta = \pi/2.$$

For  $\Gamma = 0.05$  meV,  $Q_{\text{long-lived}}''(\theta) < 0$  suggests optimal resonance trapping with a maximized Q factor of the long-lived mode at  $m\theta = \pi/2$  (see Figure S1A). We term this behavior as an “external coupling-dominated regime”. In contrast, for  $\Gamma = 0.015$  meV,  $Q_{\text{long-lived}}''(\theta) > 0$  (see Figure S1B), suggesting a compromised resonance trapping with a degraded Q factor of the long-lived mode at  $m\theta = \pi/2$  due to inter-modal coupling. We consider this behavior as the regime affected by both external and internal coupling.

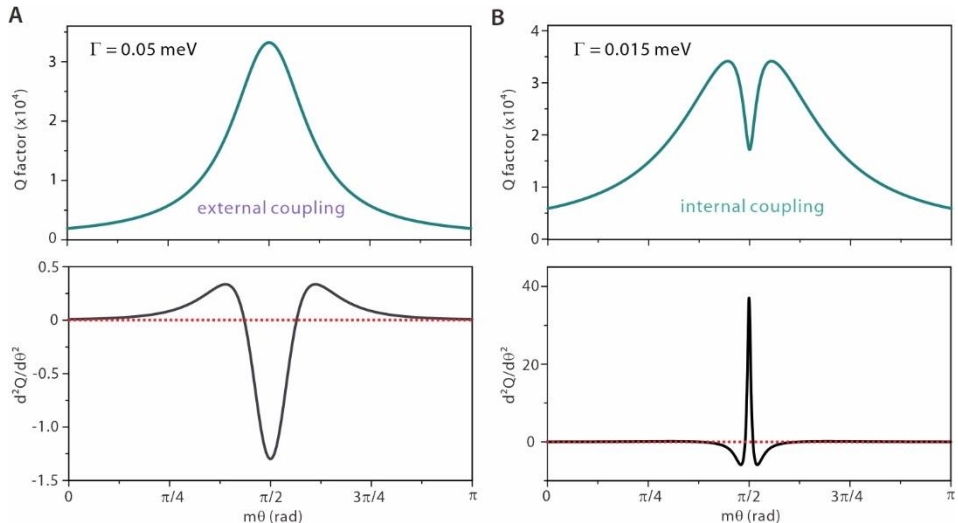


**Figure S1.** Modeled Q factor (top) and its second-order derivative (bottom) as a function of  $m\theta$  for the long-lived modes upon  $\Gamma = 0.05$  meV (A) and  $0.015$  meV (B).

## Note S2: Contributions of random dissipative coupling

For the calculations in Figure 2 in the main article, we adopted values of  $\mathbf{V}_e = -0.15$  meV,  $\mathbf{U}_e = -0.14$  meV, and set  $\mathbf{V}_o = \mathbf{U}_o = 0$ . Notably, the potential contribution of “random” dissipative coupling that does not radiate via the same channel, i.e.,  $\text{Im}(\mathbf{V}_e)$  and  $\text{Im}(\mathbf{U}_e)$ , was neglected. In this section, we elaborate on the generalized scenario considering the presence of  $\text{Im}(\mathbf{V}_e)$  and  $\text{Im}(\mathbf{U}_e)$ .

The discussion starts with solely the random dissipation effect, setting external coherent coupling via the continuum to zero ( $\Gamma = 0$ ). Here, we set  $\mathbf{V}_e$  and  $\mathbf{U}_e$  with a clear difference, with  $\mathbf{V}_e$  of  $-0.2-0.2i$  meV and  $\mathbf{U}_e$  of  $-0.1-\Delta U-0.01i$  meV, where  $\Delta U$  gets adjusted. Numerical calculations of the eigenvalue surfaces in the  $\Delta U-\theta$  parameter space are shown in Figure S2A-B.

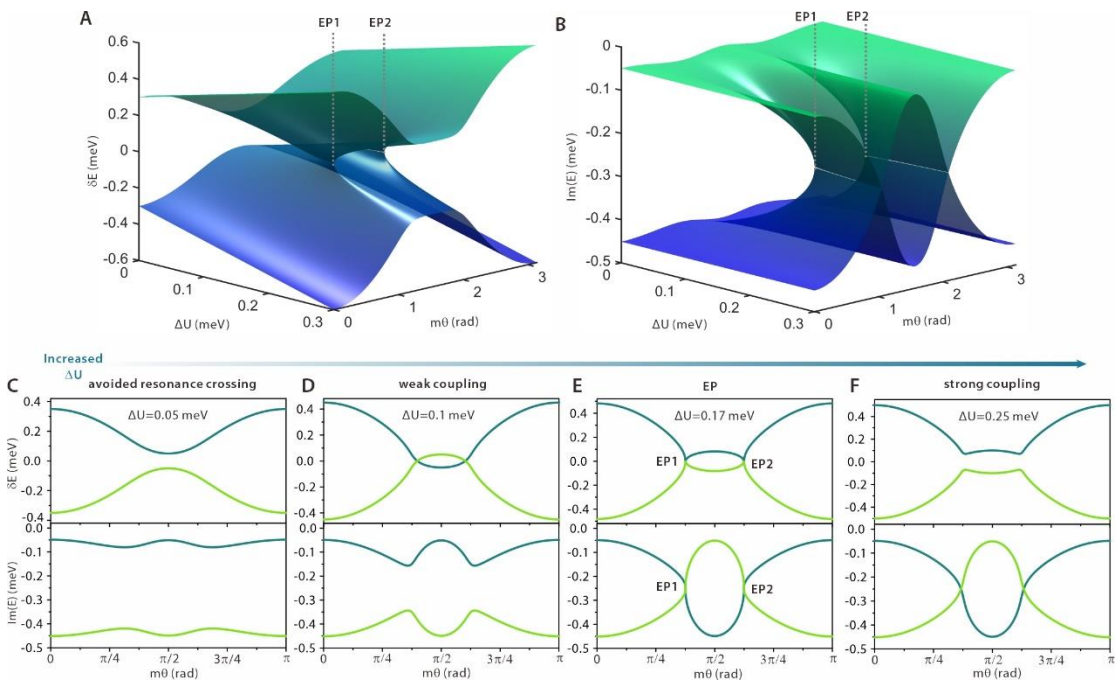


**Figure S2. Evolution of eigenvalues in the  $\Delta U-m\theta$  parameter space under random dissipative coupling.** (A-B) Numerically calculated eigenvalue surfaces in the  $\Delta U-\theta$  parameter space, including the offset in the real part  $\delta E$  (A) and the imaginary part  $\text{Im}(E_{\pm})$  (B). Here, external coupling is not considered, i.e.,  $\Gamma = 0$ . (C-F) Calculated  $\delta E$  and  $\text{Im}(E_{\pm})$  of the mode pair as a function of  $\theta$  for different  $\Delta U$  of 0.05 meV (C), 0.01 meV (D), 0.17 meV (E), and 0.25 meV (F).

When there is a significant difference between  $\mathbf{V}_e$  and  $\mathbf{U}_e$  ( $\Delta U = 0.05$  meV, see Figure S2C), a clear “avoid resonance crossing” (ARC) behavior in both the real and imaginary parts of the eigenvalues is discerned. Without the effect of external coupling ( $\Gamma = 0$ ), resonance trapping cannot be generated. By increasing  $\Delta U$  to 0.1 meV, the effect of weak internal coupling emerges in Figure S2D. The modulation of  $\theta$  results in a spectral crossing in the real part ( $\delta E = 0$ ) and an avoided crossing in the imaginary part. Upon  $\Delta U$  of 0.17 meV in Figure S2E, the system reaches two exceptional points (EPs), namely, EP1 ( $\mathbf{A} = 0$ ) and EP2 ( $\mathbf{B} = 0$ ) at  $m\theta_1 = 1.183$  rad and  $m\theta_2 = 1.960$  rad, respectively, meanwhile satisfying  $|\mathbf{V}_e^2 + \mathbf{U}_e^2 + 2\mathbf{V}_e\mathbf{U}_e \cos(2m\theta)| = 0$ . As  $\Delta U$  further increases to 0.25 meV (see Figure S2F), the modulation  $\theta$  results in an anti-crossing feature in the real part ( $\delta E > 0$ ) and meanwhile crossing in the imaginary part, certifying the strong coupling characteristics.

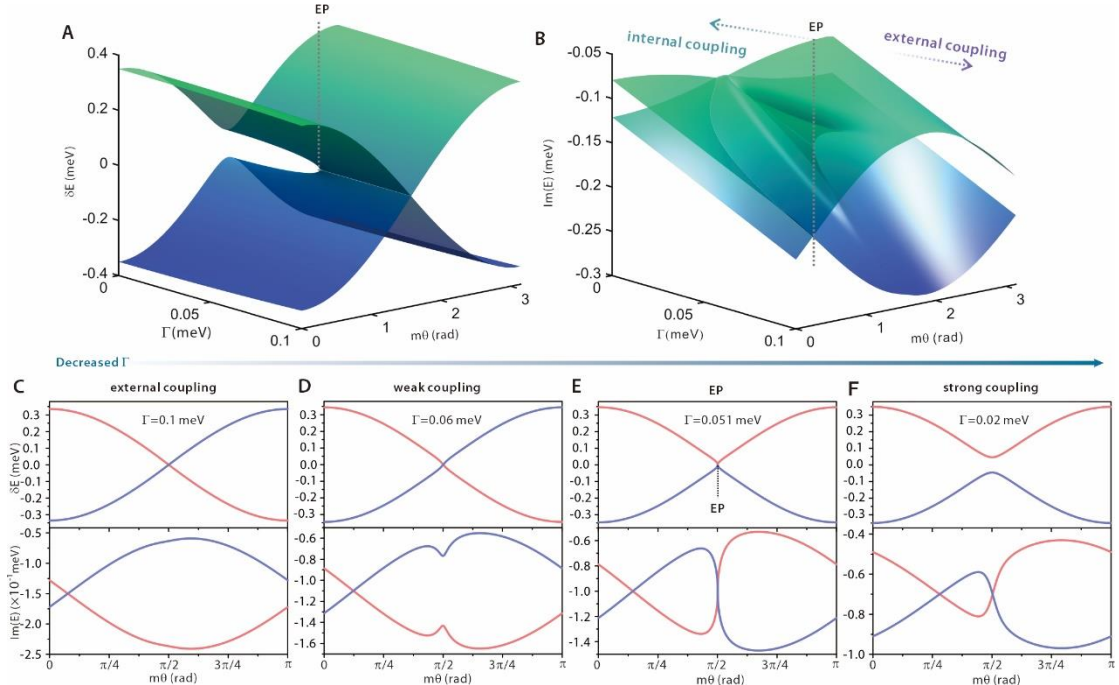


**Figure S3. Evolution of eigenvalues in the  $\Gamma$ - $m\theta$  parameter space under random dissipative coupling.** (A-B) Numerically calculated eigenvalue surfaces in the  $\Gamma$ - $\theta$  parameter space, including the offset in the real part  $\delta E$  (A) and the imaginary part  $\text{Im}(E_{\pm})$  (B). Here we set  $\mathbf{V}_e = -0.2 - 0.01i$  meV and  $\mathbf{U}_e = -0.15 - 0.011i$  meV. (C-F) Calculated  $\delta E$  and  $\text{Im}(E_{\pm})$  of the mode pair as a function of  $\theta$  for different  $\Gamma$  of 0.1 meV (C), 0.06 meV (D), 0.051 meV (E), and 0.02 meV (F).

The generalized case takes into account the radiative damping of random dissipation shown in Figure S2 and coherent external coupling via the same radiation continuum. Figure S3A-B presents numerical calculations of the eigenvalue surfaces in the  $\Gamma$ - $\theta$  parameter space. One should note that this differs from the ideal case in Figure 2 in the main text by setting non-zero values for  $\text{Im}(\mathbf{V}_e)$  and  $\text{Im}(\mathbf{U}_e)$ .

Figure S3C-F summarizes the evolutions of the mode pair while the contribution of random dissipative terms  $\text{Im}(\mathbf{V}_e)$  and  $\text{Im}(\mathbf{U}_e)$  are considered. For comparison, Figure S4 summarises the results without the effect of random dissipative coupling. While  $\Gamma$  is sufficiently large ( $> 0.1$  meV), one can identify clear resonance trapping induced by external coupling (see Figures S3C and S4A). Unlike the matching between the optimal resonance trapping point and the zero-detuning point ( $\delta E = 0$ , at  $m\theta = \pi/2$ ) in Figure S4A, the misalignment is induced due to the contribution of additional angle-dependent dissipative coupling.

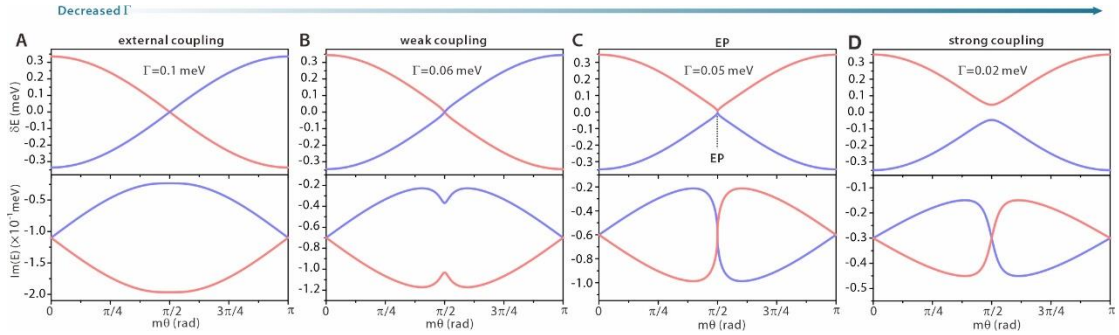


**Figure S4. Evolution of eigenvalues in the absence of random dissipative coupling.**

(A-D) Calculated  $\delta E$  and  $\text{Im}(E_{\pm})$  of the mode pair as a function of  $\theta$  for different  $\Gamma$  of 0.1 meV (A), 0.06 meV (B), 0.05 meV (C), and 0.02 meV (D). Here the random dissipative terms are neglected by setting  $\text{Im}(\mathbf{V}_e) = \text{Im}(\mathbf{U}_e) = 0$ .

As  $\Gamma$  decreases to 0.06 meV, mode hybridization emerges with  $\text{Im}(E_{\pm})$  approaching each other at  $m\theta = \pi/2$  (see Figures S3D and S4B). Furthermore, by balancing the strength between internal and external coupling terms, an EP can be reached (at  $\Gamma = 0.051$  meV in Figure S3E and at  $\Gamma = 0.05$  meV in Figure S4C) in both cases. In the case that  $\Gamma$  is sufficiently weak (0.02 meV), the system enters the strong coupling regime, presenting an avoided crossing in the real part and crossing for  $\text{Im}(E_{\pm})$ . Interestingly,

unlike the single crossing point for  $\text{Im}(E_{\pm})$  in Figure S4D, an additional crossing around  $m\theta = 0.8 \text{ rad}$  appears in Figure S3F, which is attributed to the balancing between different dissipative terms in two modes.

### Note S3: Impact of mismatch between two radiation components

For simplicity, we set  $\gamma_e = \gamma_o$  in the Hamiltonian of the radiation coupling via the continuum in Figure 2 in the main article. In such a spiral geometry, the mode-mismatch segment may lead to unbalanced radiative strengths from two originally orthogonal components (e.g., even and odd modes), namely  $\gamma_e \neq \gamma_o$ . Here we further elaborate on this case.

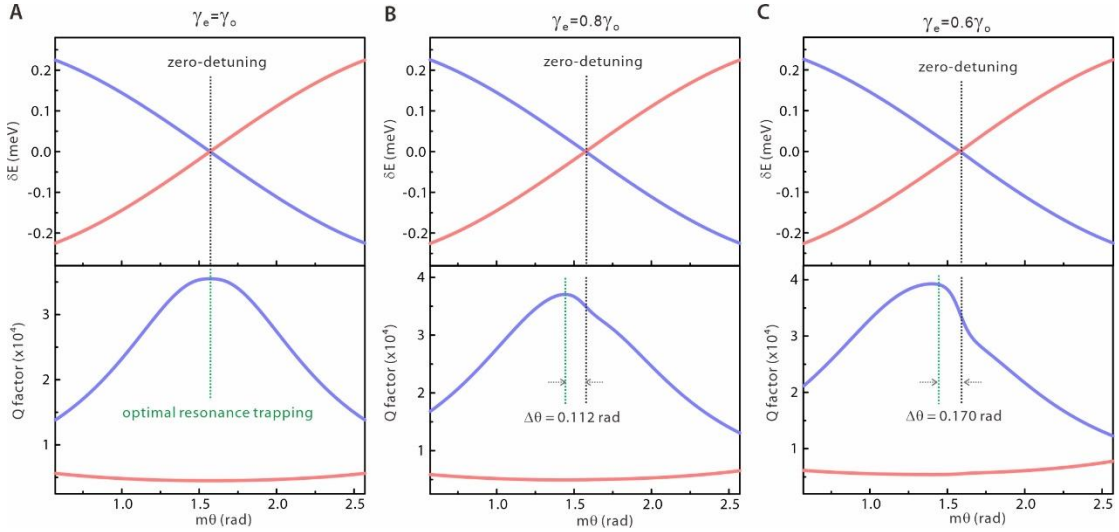


**Figure S5.** Numerically calculated evolutions of the detuning of resonant energies  $\delta E$  (top), and the Q factors (bottom) as a function of  $m\theta$  upon different  $\gamma_e$  and  $\gamma_o$ . (A)  $\gamma_e = \gamma_o$ . (B)  $\gamma_e = 0.8\gamma_o$ . (C)  $\gamma_e = 0.6\gamma_o$ .

By adopting the same set of parameters in Figure 2 in the main text ( $V_e = -0.15$  meV,  $U_e = -0.14$  meV, and  $\gamma_e = 0.05$  meV), the evolution of mode coupling is revisited by adjusting the contrast between  $\gamma_e$  and  $\gamma_o$ . For  $\gamma_e = \gamma_o$  in Figure S5A, resonance trapping with maximal Q factor is obtained at the exact zero-detuning point ( $\delta E = 0$  at  $m\theta = \pi/2$ ). As the difference between  $\gamma_e$  and  $\gamma_o$  emerges ( $\gamma_e = 0.8\gamma_o$  in Figure S5B and  $\gamma_e = 0.6\gamma_o$  in Figure S5C), one can discern a misalignment between the optimal resonance trapping point and the zero-detuning point. This is attributed to the extra modulation term  $2\Delta\Gamma V_e + 2\Delta\Gamma U_e \cos(2m\theta) + \Delta\Gamma^2$  in equation S15.

#### Note S4: Husimi projections for different coupling regimes

In addition to the results of Husimi projection for the regime dominated by external coupling presented in Figure 3B in the main article, here Husimi projections for other coupling regimes are provided in Figure S6.

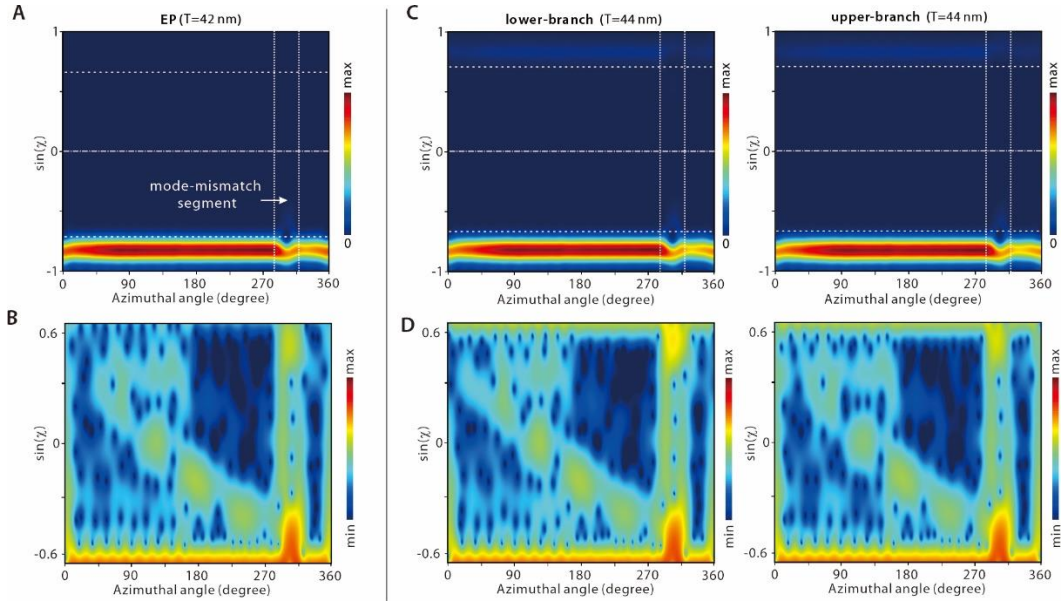


**Figure S6. Extracted Husimi projections for different coupling regimes.** (A) Extracted internal emerging Husimi functions at EP. The dashed lines indicate the critical angle for total internal reflection. The positive region ( $\sin(\chi) > 0$ ) stands for CW components whereas the negative region ( $\sin(\chi) < 0$ ) stands for CCW components. (B) Zoomed-in view of the leaky region in (A) on a log scale. (C) Extracted internal emerging Husimi functions for a strongly hybridized mode pair, including the lower branch (left) and upper branch (right). (D) Zoomed-in view of the leaky region in (C) on a log scale.

The coupling regimes get switched by varying the lateral offset of the mode-mismatch segment  $T$ . At EP, the extracted Husimi function at EP reveals the maximal mode chirality with zero CW component (see Figure S6A and B). The zoomed-in view of the leaky region below the critical lines certifies the main contribution from the mode-mismatch segment (with an azimuthal angle between  $\sim 285^\circ$  and  $\sim 317^\circ$ ). For strong coupling ( $T = 44$  nm), the extracted Husimi projections in Figure S6C indicate the preserved strong mode chirality. As presented in Figure S6D, the comparable leakage channels for the two strongly hybridized modes sharply contrast the distinct leakage channels for the short-lived and long-lived modes in Figure 3C in the main article.

### Note S5: Evolution of mode chirality across different coupling regimes

The evolution of mode chirality across different coupling regimes is analyzed in the  $\Gamma-m\theta$  parameter space in Figure S7. The mode chirality is quantified using the following expression:

$$\alpha = \frac{|\mathbf{A}| - |\mathbf{B}|}{|\mathbf{A}| + |\mathbf{B}|}, \quad (\text{S16})$$

In the conventional regime of internal coupling, significant modulation of chirality upon varying  $m\theta$  is observed. It reaches its maximum value of 1 while the system approaches the EP (i.e.,  $\Gamma = |\mathbf{V}_e - \mathbf{U}_e|$ ). As  $\Gamma$  further increases (e.g.,  $\Gamma \sim 0.05$  meV), entering the external coupling regime, the mode chirality gets gradually stabilized around  $\sim 0.22$ , indicating reinforced robustness against variations in  $m\theta$ . Such a moderate yet stable mode chirality agrees with the observation in the Husimi projection (see Figure S6C-D) in Section. 4.

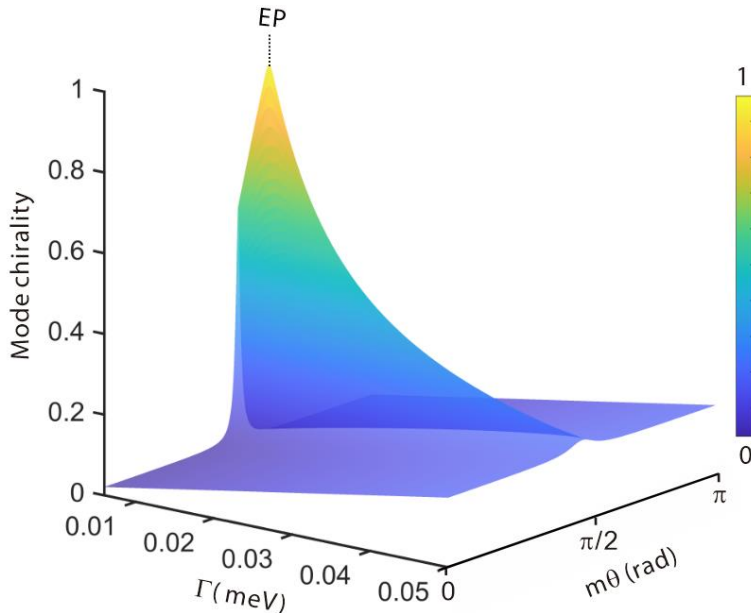


**Figure S7.** Numerically calculated surface of mode chirality in  $\Gamma-m\theta$  parameter space.

### Note S6: Supplemental analysis on the emitter-resonator system

Here we elaborate on the generalized case that a single dipole emitter is embedded in a WGM cavity, we assume that the emitter efficiently couples to both the CW and CCW propagating modes. The system dynamics can be described by a Hamiltonian in a  $3 \times 3$  matrix<sup>6</sup>:

$$H_{\text{dipole-cavity}} = \begin{pmatrix} \mathbf{E} & \mathbf{A} & Je^{-i\phi} \\ \mathbf{B} & \mathbf{E} & Je^{i\phi} \\ Je^{i\phi} & Je^{-i\phi} & \mathbf{E}_{\text{dipole}} \end{pmatrix}, \quad (\text{S17})$$

where  $\mathbf{J}$  represents the coupling strength at a particular transverse location along the cavity, and the real part of  $\mathbf{E}_{\text{dipole}}$  corresponds to the transition energy between the ground and excited states of the dipole emitter, while the imaginary part represents its decay rate. The phase  $\phi$  denotes the accumulated optical phase between the dipole emitter and a chosen reference point in the cavity.

Assuming that the intrinsic loss of the cavity modes  $\text{Im}(\mathbf{E})$  is much larger than both  $\text{Im}(\mathbf{E}_{\text{dipole}})$  and  $\mathbf{J}$ , the system operates in the weak coupling regime. In this case, strong hybridization does not occur between the dipole and the cavity modes, and the emission from the dipole rapidly couples into the WGM modes. Under this approximation, the dynamics of the dipole-cavity system reduce to:

$$i \frac{d}{dt} \begin{pmatrix} a_{CCW} \\ a_{CW} \end{pmatrix} = \begin{pmatrix} \mathbf{E} & \mathbf{A} \\ \mathbf{B} & \mathbf{E} \end{pmatrix} \begin{pmatrix} a_{CCW} \\ a_{CW} \end{pmatrix} + J \begin{pmatrix} e^{-i(\frac{E_{\text{dipole}}}{\hbar}t+\phi)} \\ e^{-i(\frac{E_{\text{dipole}}}{\hbar}t-\phi)} \end{pmatrix}, \quad (\text{S18})$$

where  $a_{CCW}$  ( $a_{CW}$ ) represents the amplitude distribution of the CCW (CW) mode.

This approximate model has been widely validated in quantum-dot-resonator systems<sup>2, 6</sup>. For our experimental studies of defect-state-enabled emission, we adopt the same model with the same approximation. The photoluminescence from the assemblies of local defects couples primarily into the CW and CCW modes. The cavity-enhanced spontaneous emission is proportional to the build-up intensity, and hence can be analyzed using temporal coupled-mode theory (TCMT).

### Note S7: Mode-dependent resonance trapping

This section elaborates on the dependence of resonance trapping on azimuthal mode order  $m$ . The eigenvalues of the full Hamiltonian (see equations 3-6 in the main article) can be expressed as:

$$E_{\pm}(m) = E_0(m) - i\gamma_0 - i\frac{\gamma_e + \gamma_o}{2} + \mathbf{V}_e + \mathbf{U}_e \pm \sqrt{\mathbf{A}(m)\mathbf{B}(m)}, \quad (\text{S19})$$

$$\text{with } \mathbf{A}(m)\mathbf{B}(m) = \mathbf{V}_e^2 + \mathbf{U}_e^2 + 2\mathbf{V}_e\mathbf{U}_e \cos(2m\theta) - \Gamma^2 - 2i\Gamma\mathbf{U}_e \sin(2m\theta), \quad (\text{S20})$$

where  $E_0(m)$  is the eigenenergies corresponding to the mode order. Equation S19 can be written in the following form:

$$\sqrt{\mathbf{A}(m)\mathbf{B}(m)} = \sqrt{\mathbf{V}_e^2 + \mathbf{U}_e^2 - \Gamma^2 + C\mathbf{U}_e \sin(2m\theta + \psi)}, \quad (\text{S21})$$

where  $C$  and  $\psi$  are jointly determined by  $\mathbf{V}_e$  and  $\Gamma$ .

As revealed in equations S19 and S21, for simplicity, assuming  $\mathbf{V}_e$ ,  $\mathbf{U}_e$ , and  $\Gamma$  are constant, then optimal resonance trapping can be reached when  $m\theta$  equals an integer multiple of  $\pi$ .

One can find nice consistency of the discernable period  $\Delta m$  in the experimental results in Figure 4E and 4G in the main article. To further validate our theoretical prediction, we performed numerical simulations of the mode series. A clear periodicity with  $\Delta m = 12$  was observed in both the simulated resonance shift  $\delta E$  and Q-factors (see Figure S8A), which is consistent with the experimental results in Figure 4E in the main text. The disparity of Q factors between simulation and experimental results is attributed to the simplified resonance condition in 2D simulations without considering the confinement and leakage along the axial dimension<sup>1, 4</sup>.

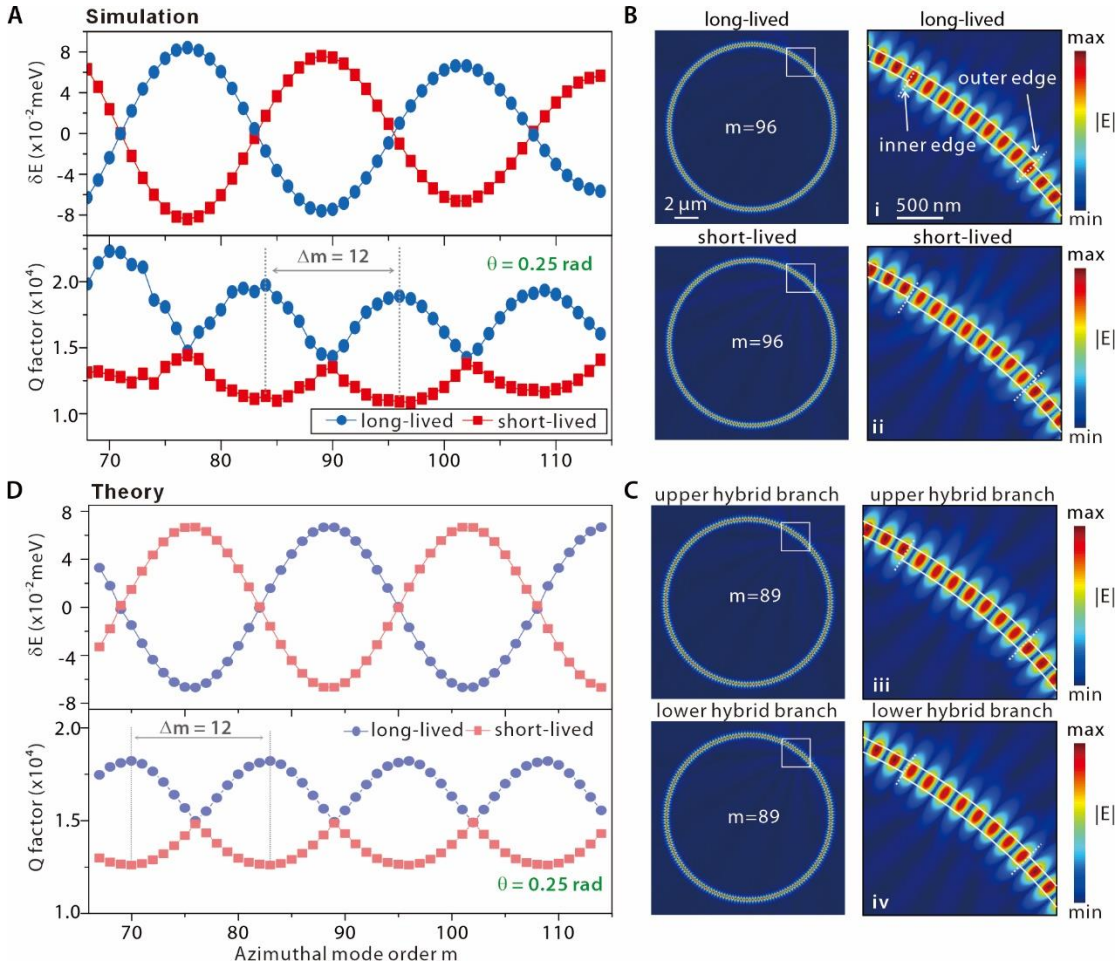


**Figure S8. Mode-dependent resonance trapping obtained from numerical simulations and theoretical analysis.** (A) Simulated  $\delta E$  (top) and Q factor (bottom) of the non-degenerate mode pair for varying  $m$ . Geometric parameters were chosen according to those from the fabricated device, including:  $\theta = 0.25$  rad,  $R = 6.9$   $\mu\text{m}$ ,  $T = 40$  nm, and  $W_R = 160$  nm. Simulated mode field distributions of the mode pairs for a spiral ring with  $\theta = 0.25$  rad for  $m = 96$  (B) and 89 (C). Insets i-iv: zoomed-in views around the mode-mismatch segment. (D) Modeled  $\delta E$  (top) and Q factor (bottom) of the mode pair upon varying  $m$  serving as a fit to simulation results. We set  $\mathbf{V}_e = -0.04 - 0.013i$  meV,  $\mathbf{U}_e = -0.03 - 0.01i$  meV,  $\Gamma = 0.02$  meV and  $\theta = 0.25$  rad.

Figure S8B-C presents the mode field distributions and radiation patterns around the mode-mismatch segment for two different mode orders as two examples revealing efficient and inefficient resonance trapping. For the mode pair at  $m = 96$  (see Figure S8B) showing a drastic contrast of Q factors, the long-lived mode displays a maximal spatial overlap between the mode anti-nodes and two spiral edges, yet generates a suppressed leakage towards the far field (see inset i). In contrast, the short-lived mode

suggests a minimal overlap between antinodes and two spiral edges, and a reinforced far-field radiation pattern (see inset ii). For  $m = 89$  (see Figure S8C), mode splitting becomes apparent. Meanwhile, the Q factors of the two modes are comparable, as evidenced by the comparable radiation patterns in insets iii-iv.

In addition to the numerical simulations in Figure S8A, the evolution can be nicely fitted using the theoretical model with predefined  $\theta = 0.25$  rad (see Figure S8D), further corroborating the theoretical model.

## Note S8: Supplemental experimental results in alternative material platforms

In addition to the experimental observation of resonance trapping in silica microtubular resonators in Figure 4 in the main article, we have observed the same phenomenon in resonators across different material platforms. Figure S9A presents the fabricated silicon nitride ( $\text{SiN}_x$ ) microtubular resonators using the dry-etching-based nanomembrane origami<sup>3</sup>. For two resonators fabricated on the same chip with slightly shifted rolling length, the characterized emission spectra in Figure S12B-C exhibit distinct modulation periods of  $\Delta m = 10$  (see Figure S9B) and  $\Delta m = 3$  (see Figure S9C), respectively, which validate the mode-dependent resonance trapping across different material platforms.

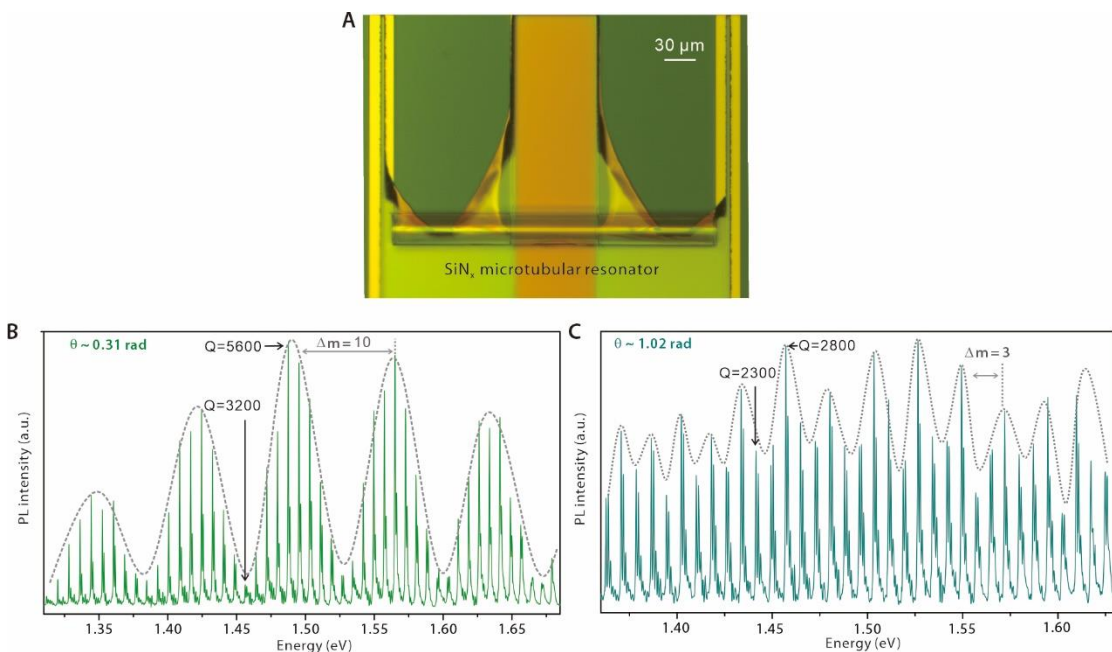


**Figure S9. Experimentally observed resonance trapping.** (A) Optical microscope image of a rolled-up  $\text{SiN}_x$  microtubular resonator. (B-C) Measured resonant spectra for two resonators with different rolling lengths, resulting  $\theta$  of 0.31 (B) rad and 1.02 (C) rad, respectively.

**Note S9: Supplemental details on sample inspection and experimental setup.**

For fabricated microtubular resonators, the spiral edges can be characterized via the assistance of scanning electron microscopy and cut by the focused ion beam. Figure S10 reveals the existence of the inner edge, as well as the mismatch of lateral scale between the two segments.

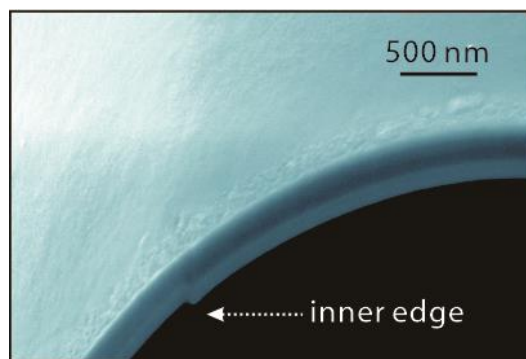


**Figure S10.** Scanning electron microscope image of a microtube after cut by a focused ion beam.

Figure S11 presents the schematic of the spectrum acquisition. More details can be found in the *Methods* section of the main article.

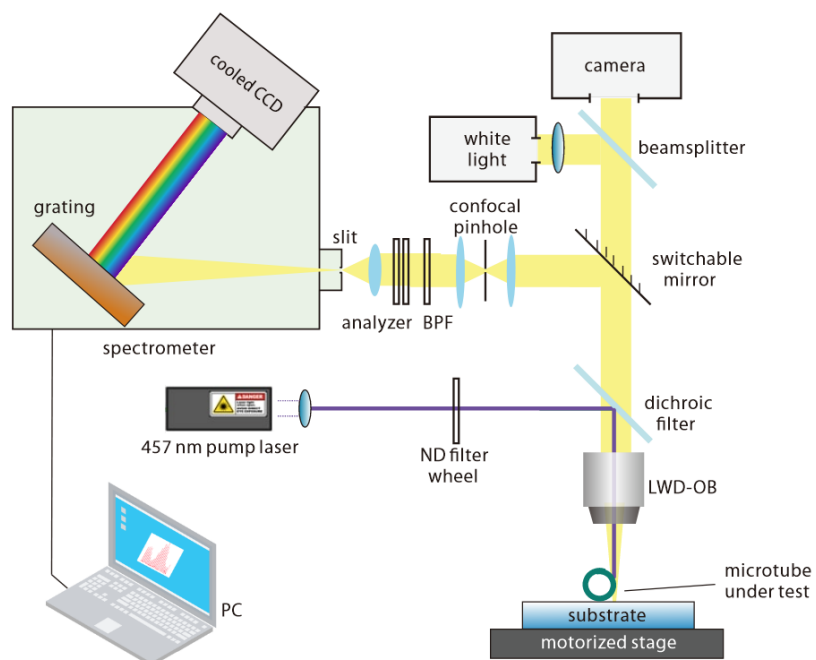


**Figure S11.** Schematic of the experimental setup. BPF: bandpass filter. LWD-OB: long working distance objective lens. ND filter: neutral-density filter.

## **Supplemental Reference**

1. Kipp, T., Welsch, H., Strelow, C., Heyn, C., and Heitmann, D. (2006). Optical modes in semiconductor microtube ring resonators. *Phys. Rev. Lett.* *96*, 077403.
2. Lu, Y., Zhao, Y., Li, R., and Liu, J. (2022). Anomalous spontaneous emission dynamics at chiral exceptional points. *Opt. Express* *30*, 41784-41803.
3. Saggau, C.N., Gabler, F., Karnaushenko, D.D., Karnaushenko, D., Ma, L., and Schmidt, O.G. (2020). Wafer-scale high-quality microtubular devices fabricated via dry-etching for optical and microelectronic applications. *Adv. Mater.* *32*, 2003252.
4. Strelow, C., Schultz, C.M., Rehberg, H., Sauer, M., Welsch, H., Stemmann, A., Heyn, C., Heitmann, D., and Kipp, T. (2012). Light confinement and mode splitting in rolled-up semiconductor microtube bottle resonators. *Phys. Rev. B* *85*, 155329.
5. Wiersig, J. (2011). Structure of whispering-gallery modes in optical microdisks perturbed by nanoparticles. *Phys. Rev. A* *84*, 063828.
6. Zhong, Q., Hashemi, A., Özdemir, S.K., and El-Ganainy, R. (2021). Control of spontaneous emission dynamics in microcavities with chiral exceptional surfaces. *Phys. Rev. Res.* *3*, 013220.
7. Zhu, J., Ozdemir, S.K., Xiao, Y.-F., Li, L., He, L., Chen, D.-R., and Yang, L. (2009). On-chip single nanoparticle detection and sizing by mode splitting in an ultrahigh-Q microresonator. *Nat. Photon.* *4*, 46-49.